Seismic Investigations of the Sun and Solar-Like Stars

Elizabeth George

A thesis submitted to
The University of Birmingham
for the degree of
MASTER OF PHILOSOPHY

School of Physics and Astronomy
The University of Birmingham
July 2012

Abstract

This thesis presents two different studies using the processes of helio & asteroseismology. In the first study we present a method for identification of the angular degree in stars where only one even and one odd ridge are seen when plotted on an échelle diagram. Three methods are discussed which use comparison techniques in an attempt to obtain an identification for a newly observed star to one where the identity of the degree is already known. The first two methods prove to be successful when tested on model data but require prior knowledge of the radial order of a mode. The third replaces the radial order with a reduced frequency. When tested on 1005 model pairs of stars this last method successfully identifies the angular degree in 1003 cases or 99.8%. This method is also able to withstand the addition of noise to the modeled frequencies. When noise of order 1 μHz is added to the model frequencies the method correctly identifies angular degree in 96.9% of cases.

The second study investigates changes with the Sun that could cause or be caused by the most recent solar minimum which was longer and quieter than expected. We have compared data collected from the Birmingham Solar-Oscillation Network during the minima of three solar cycles. Frequency differences are created between modes of oscillation observed by BiSON in the most recent minima and the two before. These data show a frequency dependent frequency shift. This type of oscillatory frequency shift suggests a sharp change has occurred in the outer regions of the Sun. Though comparisons between the observed data and model frequencies we can show that this frequency shift is consistent with a change in Γ_1 at a depth within the Sun of 0.015 $R_\odot$ which is around

the depth of the second helium ionisation zone.

Acknowledgements

Thanks go to my supervisors, Professor Bill Chaplin and Professor Yvonne Elsworth, for their support advice and encouragement during my time in the group. I must also thank my parents, sister and grandparents for their endless support and encouragement that lead me down this path in the first place. A special thanks goes to my husband, Samuel, for his constant understanding and for proof reading this thesis. I would also like to thank the members of the HiROS group, both past and present for their help and support, in particular those I've had the pleasure of sharing an office with: Kym Goss, Guy Davies and Neil Tarrant for their stimulating and enjoyable conversation.

Contents

List of Figures

List of Tables

Chapter 1

Helio & Asteroseismology

1.1 Introduction

Asteroseismology uses waves to probe the interiors of stars, just as seismology does here on Earth. The vibrations seen on the Earth are produced by earthquakes and other seismic events. The waves used for asteroseismic investigations occur naturally within many stars including the Sun and unlike on Earth they are constantly being produced. Solar oscillations were first detected in 1962 (Leighton et al., 1962). They observed localised areas of the Sun to oscillate with a period of about 5 minutes. These were thought to be localised events, and it was not until 1979 that the global nature of these models was revealed (Claverie et al., 1979). We now know that these oscillations are caused by acoustic oscillations in the interior of the Sun. The periods of these oscillations are dependent on properties of the solar interior such as temperature and composition. Accordingly, properties of the solar oscillations can hold valuable information about the internal structure of the Sun.

Pulsating stars have been observed for centuries, for example Mira was observed by David Fabricius in 1596 (e.g. Wolf, 1877). These early observations were of stars like Cepheid variables which show dramatic changes between their brightest and dimmest luminosities. These stars show a small number of large amplitude oscillations and often

only oscillate at a single frequency (e.g. Montgomery, 2011). Solar-like stars show smaller changes but oscillate in a large number of frequencies, simultaneously, providing a much wider spectrum for analysis and data extraction.

There are three different classifications of the waves produced within stellar interiors: pressure waves (p-modes), gravity waves (g-modes) and surface gravity waves (f-modes). These are named due to the respective restoring forces. Each of these waves are produced and propagate via different methods in different parts of a star.

In the Sun the most observed are pressure waves, these are excited stochastically in the upper regions of the convective zones of stars, less than 200km below the visible surface (e.g. Goode et al., 1992). This motion produces acoustic noise. The Sun is convective from about 0.7 $R_{\odot}$ to near the visible surface. Figure 1.1 shows a cut away view of the solar interior, showing the relative sizes of the three main sections of the solar interior. Large excitation events such as solar flares may also contribute to the excitation of modes. The acoustic noise produced is spread over a wide range of frequencies. Some of these frequencies will interfere constructively and become standing waves (modes of oscillations). It is these standing waves which we observe on the surface of the Sun. If these oscillations have sufficiently high amplitudes they will be viewable from the Earth.

These standing waves are trapped within an acoustic cavity. The upper boundary of such a cavity is created by the sharp change in density of the plasma at the top of the photosphere causing the waves to be reflected back into the interior. If the density scale height is smaller than the length scale of a mode then the pressure changes required to maintain the mode cannot be sustained over the length of the time of the period of the mode. The lower boundary differs in depth between modes and is illustrated in Figure 1.2. As the waves travel towards the centre of the star the speed of sound increases causing the waves to be refracted, eventually turning them round so they move back towards the surface. These acoustic waves are able to travel through both convective and radiative

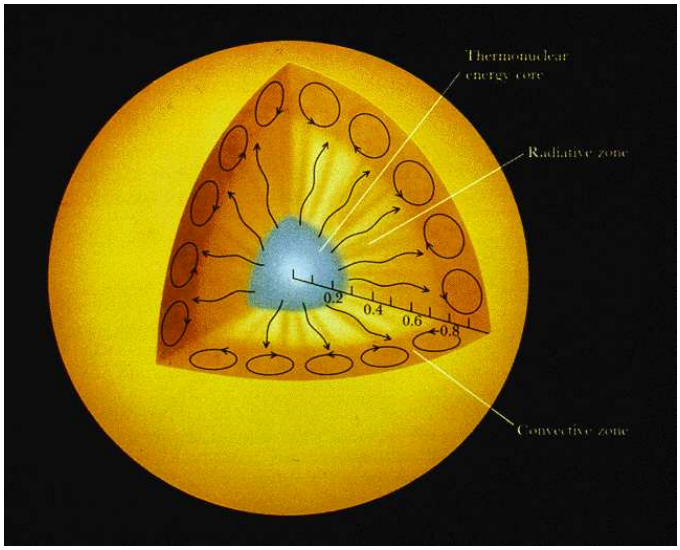

Figure 1.1: A cut away view of the solar interior showing the relative sizes of the three main sections: the core where energy is produced though nuclear fusion, the radiative zone where this energy is transported to the surface though radiative transfer and the convective envelope where convection is main means of energy transfer. Image from `http://astro.wsu.edu/worthey/astro/html/lec-sun.html`.

zones of stars so make ideal probes of stellar interiors.

Gravity waves (g-modes) are density waves with gravity (or buoyancy) as their restoring force. They occur in regions where radiative transfer is the primary means of energy transportation. In the Sun they are trapped in the central regions below the convective zone. In the radiative regions displaced parcels of gas will experience buoyancy forces that act to return the parcel to its equilibrium position. In convective regions, if a parcel of gas is displaced vertically it will continue to rise or fall preventing gravity wave propagation. In solar-like stars with a convective envelope these waves are yet to be conclusively seen, although detection of the signatures of an ensemble of g-modes has recently been claimed (Garcia et al., 2007). These modes are difficult to detect as they are confined to the radiative interior and have only residual amplitudes on the surface due to the waves being evanescent through the convective zone. These modes are of interest on solar-like stars as although they have very small amplitudes they are a more sensitive probe of the deep

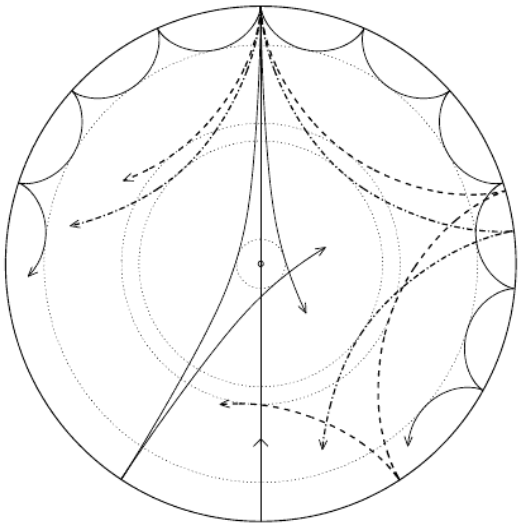

Figure 1.2: Different waves travel to different depths inside the Sun. As this plot shows the upper turning point of a wave is similar for all modes while the lower turning point is heavily dependent on angular degree. Image from Christensen-Dalsgaard (2003).

interior than p-modes. In general the frequency of g-modes are much lower than p-modes. In some cases the frequencies can become comparable; when this happens they can start to exchange their physical nature and become mixed modes (Bedding & Kjeldsen, 2003). These modes act like g-modes in the deep interior and like p-modes in the outer regions.

Surface gravity waves (f-modes) have gravity or buoyancy as a restoring force like gravity waves but differ in that they occur on the surface of a star. On the Sun they occur near or at the photosphere, the visible surface of the Sun, where convection gives way to radiation as the optimum form of energy transfer.

The simplest approximation of a star is that of a self-gravitating spherical ball of plasma in hydrostatic equilibrium. This approximation enables the horizontal structure of the modes to be expressed in terms of spherical harmonics, $\mathrm{Y}_l^m(\theta, \phi)$, where θ is the colatitude and ϕ the longitude. The angular degree, ℓ, represents the number of nodes seen on the surface and can take any integer value. The azimuthal order, m, measures the number of modes which cross the equator and intersect the poles. The azimuthal order

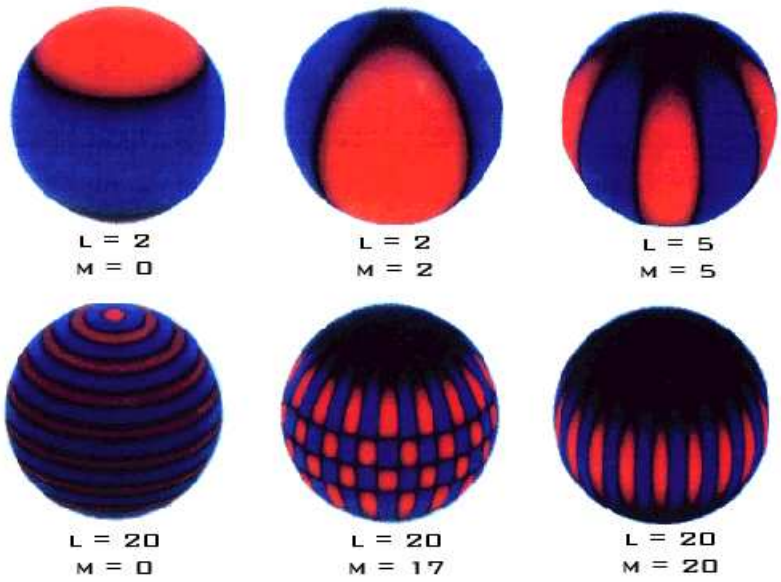

Figure 1.3: Various modes of oscillation that are present in the Sun and their corresponding identifiers. Image taken from `http://bison.ph.bham.ac.uk/background.php`

has vlaues in the range $-\ell \leq m \leq \ell$. The radial order, n, counts the number of nodes between the upper and lower turning points of the mode. By convention, acoustic p-modes have positive values of n and gravity modes have negative radial orders. For a perfect non-rotating sphere the frequency of a mode would be independent of m. This degeneracy will be broken by any departure from symmetry, rotation or the presence of a magnetic field. Figure 1.3 shows examples of 6 modes of oscillation and their corresponding ℓ and m values.

To obtain a detailed view of the interior of a star many frequencies need to be observed. In the case of the Sun, a large number of oscillations are seen, so we can build a detailed view of the interior. Each mode of oscillation produces its own signature on the solar surface and when these are added together they form a complex pattern. As each mode travels to a different depth and hence carries its own information it is important to be able to distinguish between the different modes.

1.2 What Can We Learn From Asteroseismology

The ability of helioseismolgy to probe the interior of a star has provided a large amount of information on the solar interior and the physics at work. One of the earliest triumphs of helioseismolgy was the constraint on the position of the base of the convective zone. Deubner (1975) and Gough (1977) showed that the convection zone was $\sim 50\%$ deeper than implied by conventional models. Christensen-Dalsgaard et al. (1991) found the base to be $0.713 \pm 0.003\ R_{\odot}$ from the centre of the Sun. This is in agreement with more recent findings of Basu & Antia (2004). Helioseismology is the only way to tightly constrain the depth of the convection zone.

Rotation can be seen in seismic data though the splitting of frequency peaks. The rotation of a star can alter the speed of a wave. If the wave is moving with the direction of rotation then the speed of rotation will be added to the natural speed of the wave. If moving in the opposite direction then the wave will have to work against the motion of the star producing a slower overall speed. These waves generally propagate in all directions so there will be components moving with, against and parallel to the direction of rotation. These differences in velocity cause the frequency of a mode to be split into multiple peaks. The number of peaks seen will be dependent on the angular degree. For an $\ell = 0$ mode there will be no splitting, while, for example, for an $\ell = 1$ mode three peaks will be seen. This splitting will be more pronounced the faster a star rotates giving a way to probe rotation rates within a star. This method has been used to uncover the solar rotation rate below the photosphere (Antia & Basu, 2010). The photosphere has been observed to rotate differentially though observations of sunspots. Helioseismology has enabled us to know that this differential rotation continues to the bottom of the convection zone where the Sun begins to rotate as a solid body (Chaplin et al., 1999; Garcia et al., 2004). The region where this change in rotation occurs is a region of intense shear called the tachocline.

A solution to the solar neutrino problem was found thanks to insights provided by helioseismolgy. The solar neutrino problem arose from a discrepancy between the number of neutrinos observed and the number predicted from models of the solar interior (Davis et al., 1968). The precise oscillation frequencies provided by helioseismolgy showed the problem to be with the neutrino physics and not the solar models (Elsworth et al., 1990). The accepted solution is that the neutrinos are able to change flavour. The first experiments to look for neutrinos could only measure a single flavour, so the number of neutrinos seen would be less than expected, if they are able to change to a different flavour between the Sun and the detectors on Earth. More recently, the Sudbury Neutrino Observatory in Canada has been able to detect all three flavours of neutrinos (Ahmad et al., 2001), finding that the total flux of neutrinos agrees well with solar model flux calculations (Aharmin et al., 2008).

When used in conjunction with solar models the information gained from helioseismology can be used to infer helium abundances (e.g. Serenelli et al., 2011; Delahaye & Pinsonneault, 2006). This number is important not only for solar physics but also for modelling the solar system and the Galaxy. The solar helium abundance cannot be inferred by spectroscopy as the photosphere is not hot enough to produce the required spectral lines of helium. These lines are seen in the chromosphere but the region is not in thermal equilibrium and cannot be used to infer robust abundances.

1.3 Data

The oscillations of stars are commonly observed by two different methods which look for their effects on the surface of the star. As a star oscillates it expands and contracts, causing any light emitted to be Doppler shifted. The expansion causes the visible surface to move towards the observer and the light emitted to be blue shifted. As the star

contracts and the surface moves away the emitted light is red shifted. Such changes cause the frequencies of light emitted to vary with the same frequency as the oscillation. Doppler velocity measurements are taken from observations of single lines or sometimes many, making it ideal for observations of the Sun due to the large number of bright lines which can be observed.

The expansion and contraction of the star also causes changes in the total intensity of the light emitted. As a star contracts its temperature increases causing an increase in brightness; as it expands it cools and dims. Intensity measurements over visible bands enable light from a significant range of wavelength can be used. In addition a large number of stars can be observed at once using relatively simple equipment, making intensity measurements ideal for asteroseismic investigations. Unfortunately, the Earth's atmosphere limits the precision of ground based measurements so this technique is mainly utilised in space based missions. These oscillations are small in amplitude, typically a few parts per million (e.g. Fröhlich et al., 1997).

Both methods have different sensitivity to modes of a given angular degree. In general, velocity measures are more sensitive to modes of higher angular degree. Intensity measurements are more sensitive to the granulation background as they detect temperature changes associated with these as well as the oscillations themselves. Currently, ground based observations utilize the advantages of the Doppler velocity method while space based missions are more likely to use intensity measurements. In both of these cases it is the frequency of any tiny changes which contain the desired information. This makes it sensible to perform a Fourier transform on the data. This will translate data in a time series into the frequency domain, making it easier to see periodic oscillations; this process is explained further in Section 1.3.3

1.3.1 The Kepler Space Mission

The *Kepler* space mission utilises the similarities in data needed for both planet finding and asterosiesmic observations. The mission was launched on the 6th March 2009 with the main objective of searching for Earth-like planets in orbit around Sun-like stars. This planet search is being performed via the transit method. Small periodic changes in a stars brightness can be caused by a planet passing between the host star and the observer. The light curves when sampled at a suitable cadence can also be used for asteroseismology (Gilliland et al., 2010). The information obtained from asteroseismology can also prove useful to planet finders. In particular the transit method provides a way of calculating the radius of the planet but only as a function of the radius of the star. Asteroseismology provides an accurate way to measure a star's radius which therefore helps to constrain the planet's size.

The *Kepler* mission is surveying a small section of the Milky Way Galaxy in the region of the constellations of Cygnus and Lyra. This region is highlighted in Figure 1.4. *Kepler* can observe stars down to 16th magnitude (Borucki et al., 2006). In order to have a constant view of this patch of sky the satellite has been placed in an Earth trailing heliocentric orbit.

There are also other instruments taking asteroseismic measurements from the ground and space. The first spacecraft dedicated to asteroseismology was MOST (Microvariability and Oscillations of STars) a Canadian satellite launched in 2003 (Walker et al., 2003). More recently, CoRoT (COnvection ROtation and planetary Transits) a French led Mission, has been collecting data since 2007 (Michel et al., 2008). CoRoT like Kepler and MOST looks for small changes in stellar brightness. There are also numerous telescopes on the ground involved in asteroseismic observations but there is not currently a dedicated observatory. The SONG (Stellar Observations Network Group) network hopes to change this by building a network of up to 8 telescopes positioned around the globe so targets

can be observed for long stretches of time (Grundahl et al., 2008).

1.3.2 The BiSON network

The Birmingham Solar-Oscillations Network is a network of six ground based telescopes positioned with the aim of achieving a near constant view of the Sun (Chaplin et al., 1996). They are positioned in Narrabri (New South Wales, Australia), Canarvon (West Australia), Sutherland (South Africa), Izaña (Tenerife), Las Campanas (Chile) and Mount Wilson (California, USA). Each station has a resonant-scattering spectrometer which measures the Doppler shift of light emitted by the Sun. The network has been collecting data since 1981 (Elsworth et al., 1995) and covers three solar cycles (Broomhall et al., 2012). A resonant scattering spectrometer uses light from a single emission line (in the case of BiSON the potassium D1 spectral line). The network makes Sun-as-a-star observations which means light from the entire disc is integrated to make observations of low-ℓ modes.

BiSON is not the only network of telescopes collecting helioseismic data. The Global Oscillations Network Group (GONG) is also a ground based network of 6 sites (Harvey et al., 1996). GONG like BiSON observes Doppler velocity shifts however GONG makes resolved observations so is able to observe medium- and high-degree modes. Spaced based observations have also been undertaken by the Solar and Heliopheric Observatory (SOHO) which is positioned at the L1 Lagrangian point producing a constant view of the Sun (Lemaire, 1991). Among the many instruments on board SOHO are three designed for helioseismolgy. The Global Oscillations at Low Frequencies (GOLF) instrument measures Doppler velocity measurements of the whole Sun (Gabriel et al., 1995). The Michelson Doppler Imager (MDI) made specially resolved Doppler measurements (Kosovichev et al., 1997) and the Variability and solar IRradiance and Gravity Oscillations (VIRGO) made integrated intensity measurements (Fröhlich et al., 1995). The Helioseismic and Magnetic Imager (HMI) on board the Solar Dynamic Observatory launched in 2010 and

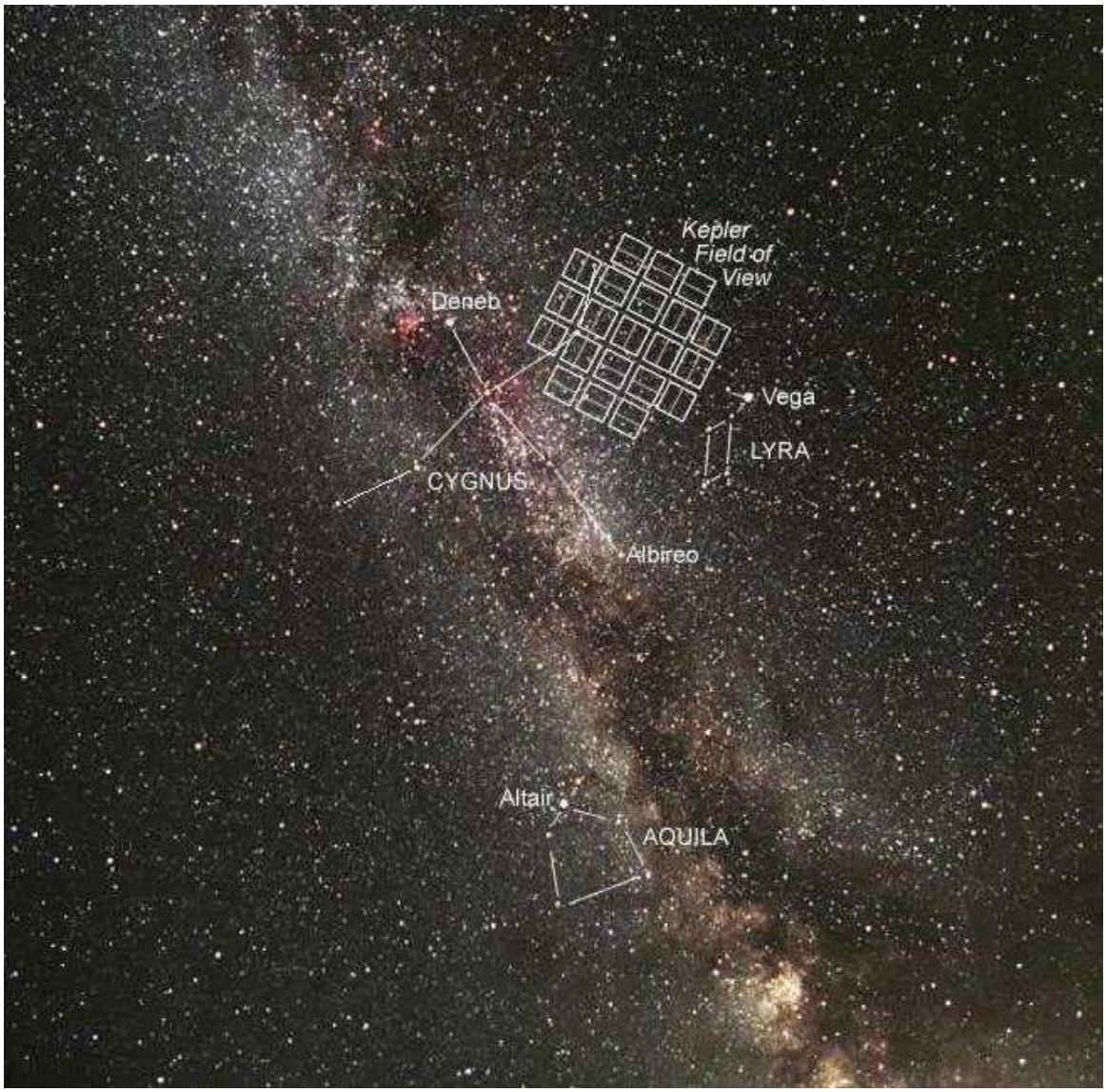

Figure 1.4: The image shows the field of view of the Kepler spacecraft in relation to the surrounding constellations and how the field of view is split into squares. Each square is formed from a pair of CCD elements of which there are a total of 42. Image from `www.nasa.gov`.

is measuring changes in Doppler velocity, intensity and vector magnetic field at the solar photosphere (Schou et al., 2012).

1.3.3 Fourier Analysis

The majority of the work in this thesis has involved using individual frequencies extracted from helio and asteroseismic data. The first step in such an extraction is to convert the data from the time to the frequency domain. This is achieved through Fourier analysis, which is a mathematical relationship between the time, $f(t)$ and frequency domains, $F(\nu)$, via:

$$F(\nu) = f(t)e^{-i2\pi\nu t}dt, \tag{1.1}$$

where ν is frequency and t is time. The Fourier transform provides a way to turn the complicated time series obtained from a star to a set of individual frequencies which appear as narrow peaks in the power spectrum (more details later in this chapter). For discrete sets of data, we use an approximate form known as the Fast Fourier Transform (FFT). This is a form that allows the transform to be performed quickly and efficiently. An FFT uses a discrete version of a Fourier transform:

$$G(\nu) = \frac{1}{N}\sum_{x=0}^{N-1} g(x)e^{-\frac{i2\pi\nu x}{N}}, \tag{1.2}$$

where N is the number of points in the time scales. $G(\nu)$ then provides the approximate Fourier transform up to the Nyquist frequency, ν_{nq}, which is defined as

$$\nu_{nq} = \frac{1}{2\Delta t}. \tag{1.3}$$

The Nyquist frequency gives the highest frequency that can be seen at a given sampling rate (Δt). The resolution of a frequency-power spectrum is determined by the length of

the time series, T,

$$\Delta\nu = \frac{1}{T}, \tag{1.4}$$

so the longer a time series the better the resolution.

1.3.4 Power Spectra

The most natural way to visualise the collected data is in the form of a power spectrum of the Fourier transform. This may be shown visually as a plot of frequency against power and shows the position and strength of different modes of oscillation. Figure 1.5 shows an example of such a plot created from unresolved oscillation measurements of the Sun. Whole Sun oscillations are seen when intensity or Doppler shift measurements are collected for the entire disc of the Sun's visible surface are observed. This has the effect of averaging out modes of high degree leaving the observer predominately with components from ℓ=0, 1, 2 and 3. The practice of collecting light from the entire disc of the Sun is also know as Sun-as-a-star observations (e.g. Salabert et al., 2009). As we are unable to resolve the discs of other stars, asterosiesmic observations are always of low degree modes. These modes pass through the deep interior of the Sun and so provide a probe of the Sun's core. The power spectrum seen in Figure 1.5 has been created from data collected by BiSON. The data were collected over an approximately four month period. It shows a highly regular frequency structure, which is clearly visible in the second part of the figure. Here the $\ell = 0$ and $\ell = 1$ modes have been labelled. Each peak also has a neighbour, which have angular degrees of $\ell = 2$ and $\ell = 3$ respectively. This regular spacing leads to two types of frequency spacing, the large and small separations. The large separation ($\Delta\nu$) is the difference in frequency between adjacent radial orders of the same angular degree,

$$\Delta\nu_{(\ell)} = \nu_{(\ell,n+1)} - \nu_{(\ell,n)}. \tag{1.5}$$

This value is mainly dependent on the time it takes for sound to travel between the centre and the surface of the Sun. The small frequency separation ($\delta\nu$) is predominantly dependent on the sound speed gradient in the core. The small separation, is the difference between pairs of even and odd modes,

$$\delta\nu_{(\ell,\ell+2)} = \nu_{(\ell,n)} - \nu_{(\ell+2,n-1)}. \tag{1.6}$$

This can be calculated for the pairs of 0, 2 or 1, 3. The same equations apply to other stars. We expect the oscillation spectra of other solar-like stars to have the same features as the solar oscillations spectra shown in Figure 1.5.

Taken together the large and small separations can be used to produce an asteroseismic Hertzsprung-Russell diagram (also known as a Christensen-Dalsgaard diagram) which can be used to determine the age and mass of a star (assuming the composition of the star is known), as illustrated in Figure 1.6.

1.3.5 Échelle Diagrams

The échelle diagram can be used to identify the angular degree of an observed frequency. This process was first suggested by Grec et al. (1983) and used to identify the degree of solar modes. The process involves splitting a spectrum into lengths of the star's large separation which are then stacked on top of each other. This process has the effect of lining up frequencies into ridges corresponding to different angular degrees. Figure 1.7 shows an example of an échelle plot created from frequencies found in data collected by BiSON between May 2008 and April 2009. In this figure we can see that the frequencies are split into four distinct regions. Échelle diagrams can also be created from the power spectra. An example of such a plot can be seen in Figure 1.8 here the ridges are seen as an increase in power. This power increase marks the position of the frequencies observed

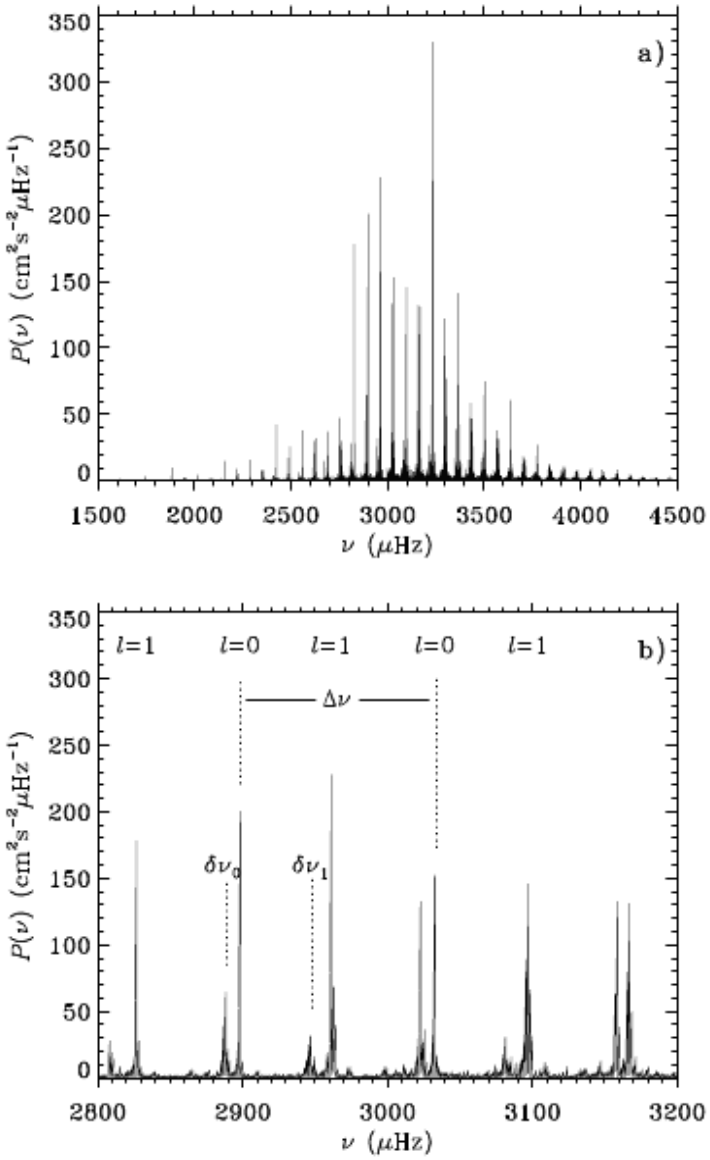

Figure 1.5: Power spectrum showing low degree modes. The data were collected using the BiSON network which records Doppler velocity measurements of integrated light from the disk of the Sun. Figure 1.5(b) shows an expanded view of the central frequency range of Figure 1.5(a). Here some of the modes have been labelled with their angular degree. The large and small separations have also been marked. Image taken from Christensen-Dalsgaard (2003).

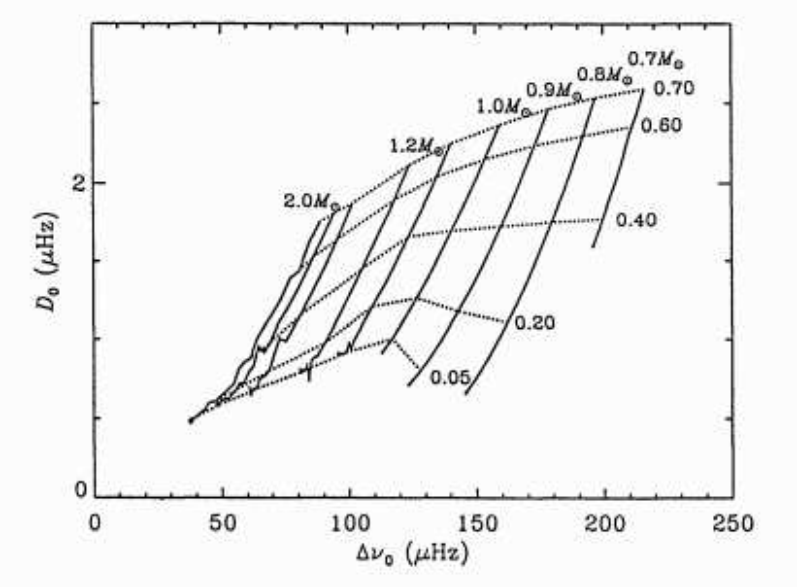

Figure 1.6: The asteroseismic HR diagram is used to help determine the age and mass of a star. Figure taken from Christensen-Dalsgaard (1993).

to oscillate on the star.

1.4 Solar Cycle

Aristotle thought that the Sun was a never changing perfect sphere (Burent, 1928). We now know that the Sun is far more interesting with structure and activity that changes over time. The first structures seen on the surface of the Sun were sunspots. Galileo made a series of sunspot observations in 1612 (Galileo, 1613). These are regions of intense magnetic field where the temperature of the photosphere is relatively cool so they appear as dark spots on the surface of the Sun. The number of spots seen on the Sun is not constant but varies over an 11 year cycle which was discovered by Schwabe (1843). The first sunspots of a cycle will appear at latitudes of about 30 degrees in both hemispheres, as the cycle progresses and the number of spots increases the sunspots appear closer to the equator. Figure 1.9 shows the variation in sunspot position on the solar surface. This

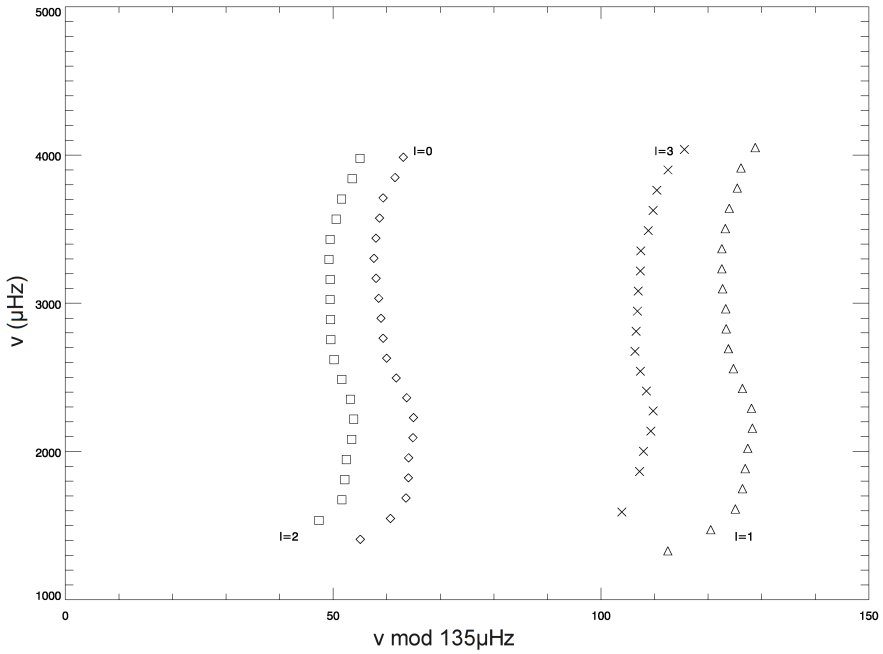

Figure 1.7: Figure showing an échelle plot created from frequencies found in solar data collected by the BiSON network between May 2008 and April 2009. Here we can see that the frequencies are split into four ridges. From left to right the ridges are paired $\ell = 2$ then $\ell = 0$. Followed by the odd pair of $\ell = 3$ and $\ell = 0$.

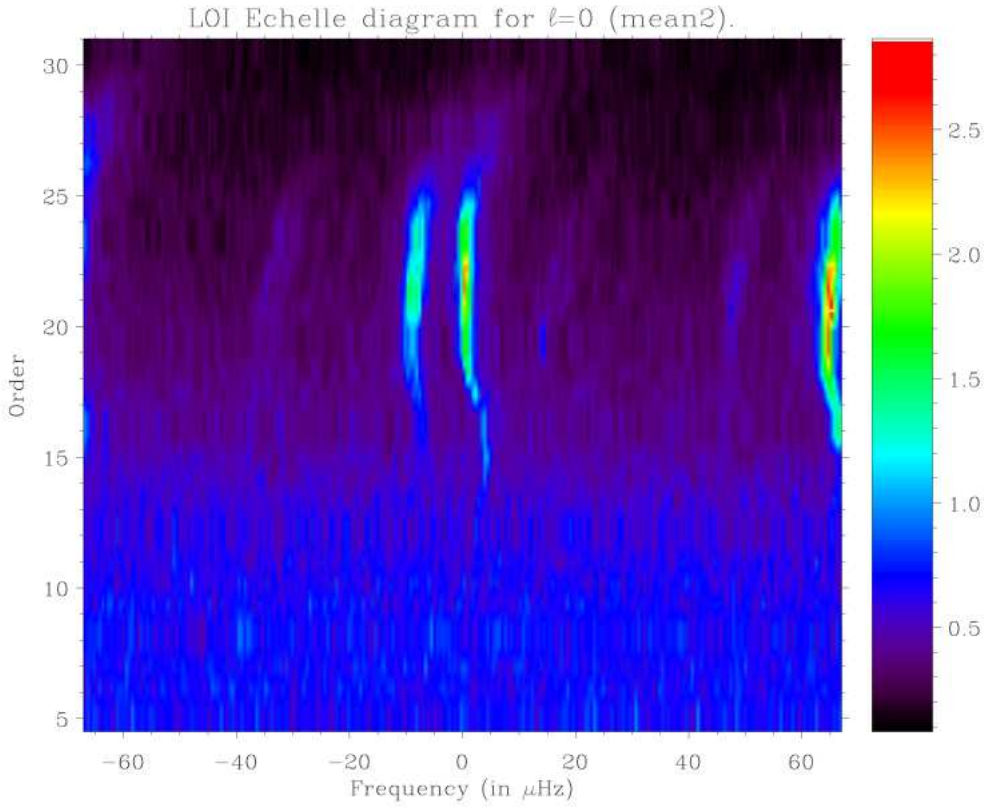

Figure 1.8: Figure showing an échelle plot created from solar data collected by the Luminosity Oscillations Imager (LOI) on board the Solar and Heliospheric Observatory (SOHO). Figure from Appourchaux et al. (1998).

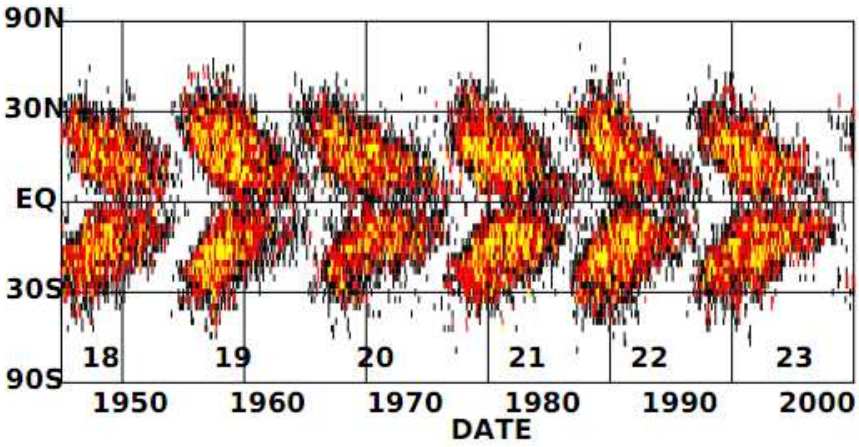

Figure 1.9: Butterfly Diagram showing how the position and number of sunspots on the Sun varies with time. Image from Hathaway (2011).

is a plot known as the butterfly diagram where sunspot latitude is plotted against time.

The cycle has been shown to follow changes in the Sun's magnetic field (Hale, 1924). The Sun begins a cycle with a poloidal magnetic field much like the Earth's, but unlike the Earth the Sun's outer layers rotate differentially with the equator rotating with a period of ∼25 days and the poles ∼35 days. This differential rotation pulls the magnetic field lines of the Sun with it and wraps them around the Sun, taking the Sun's magnetic configuration from a poloidal field to a near toroidal one. How the Sun returns to a poloidal field is less understood. We do, however, know that around solar maximum the magnetic poles of the Sun exchange places so North becomes South and South becomes North and consequently it takes 22 years for the Sun to return to its original state (e.g. Roshchina & Sarychev, 2011).

The solar cycle has an average duration of 11 years, though there have been notable outliers. One of the largest periods seen has been named the Maunder minimum when almost no spots were seen between 1645 and 1715 (Eddy, 1976). This coincided with a period of extremely cold temperatures. More recently, the last solar minimum was longer and quieter than expected (Jian et al., 2011).

The solar activity cycle is also seen in p-mode oscillations. The rise and fall in activity can be seen by a frequency shift observed in p-modes. Modes with frequencies below 4000 μHz are seen to increase in frequency with an increase in activity. This effect can be best shown as a frequency difference or frequency shift, i.e. by showing how the frequencies have changed by finding the difference between two sets of frequencies obtained at different epochs. Chaplin et al. (2007) looked at the difference over three cycles of BiSON data by comparing the observed frequencies to a minimum activity reference epoch (the minimum of cycle 23 which occurred around 1996). These differences were then compared to various activity proxies. There are various ways to record solar activity including Sun spot number, radio flux and solar irradiance. The 10.7cm solar radio flux originates primarily from non-thermal processes in coronal plasma trapped in the magnetic fields over active regions (Tapping, 1987). The total solar irradiance is the total amount of solar radiative energy incident on the Earth's upper atmosphere, which also increases with increasing levels of activity. Figure 1.10 shows the frequency shift with an activity proxy over plotted, in this case the 10.7cm radio flux. This plot shows a strong correlation between p-mode frequency and solar activity and that p-modes are sensitive to the same changes that produce solar activity.

1.5 Thesis Overview

This thesis presents two different pieces of research. The first looks for an automated way to identify the angular degree in asteroseismic data where only ℓ=0 and ℓ=1 modes can be distinguished. This is achieved through investigation into different comparison techniques that use stars (real or artificial) with previously defined identifications to gain information on newly observed stars. The techniques used in this thesis scale the frequencies of one star in such a way as to match the large separations of the newly observed star to the

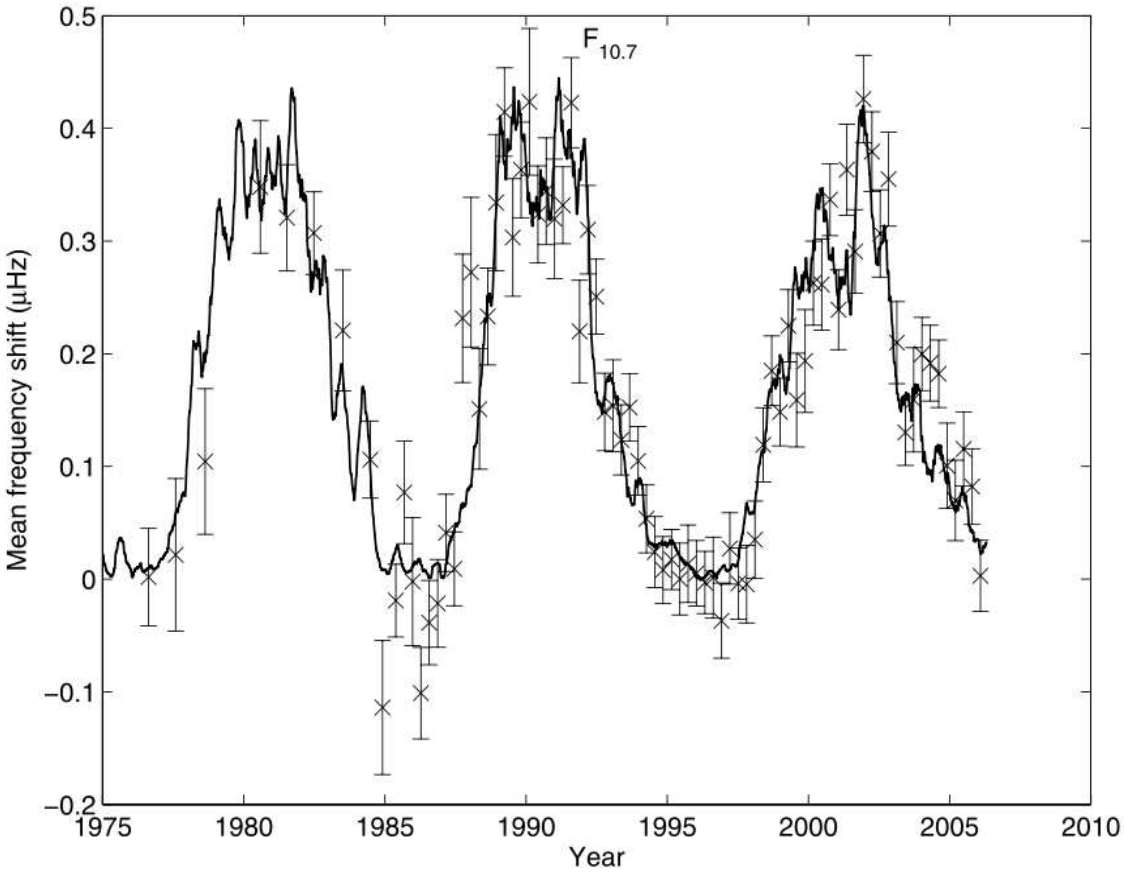

Figure 1.10: Figure from Chaplin et al. (2007) showing how p-mode frequencies change with the solar cycle (crosses) as compared to the 10.7cm radio flux (solid line) used as an activity proxy.

comparison star. The first uses a multiplicative scaling factor which enables an échelle diagram to be used to compare the frequency ridges of the two stars. The second uses an additional offset with the aim of removing any dependency on the surface terms of the two stars as this can cause the ridges on an échelle plot to shift out of an expected position. The methods mentioned above compare frequencies by matching radial order. The radial order can also be challenging to identify making a method without this requirement preferable. We achieved this by using a combination of the individual frequencies to create an dependent variable based on frequency, not radial order. All of these methods have been tested on model data where the angular degree and radial order of each frequency is known.

The other investigation presented in this report uses helioseismic data collected by BiSON to investigate the Sun's most recent extended minimum. We compare data samples from the last three solar minima. The frequency differences between these samples show periodic frequency shifts which are characteristic of an abrupt change within the solar interior. Similar signatures are seen in helioseismic data due to sharp changes in the sound speed profile at the base of the convection zone and the second helium ionization zone. In this investigation we add a similar sharp change to model data at a variety of depths. This change is applied to either sound speed, density or the first adiabatic exponent. The frequency shifts caused by applying this change have then been compared to the shift seen in the data collected by BiSON to test the likelihood of such a change being the cause of the recent extended solar minimum.

Chapter 2

Identifying the Angular Degree of a Mode

2.1 Introduction

Since the launch of spacecraft designed to detect modes of oscillation in stars other than our Sun the number and type of stars seen with oscillations has greatly increased. Observations of these stars are unresolved so only low-degree modes are observed. The *Kepler* spacecraft makes photometric observations which tend to produce weak ℓ=3 modes, producing a spectra where only ℓ=0, 1 and 2 modes are observed. When plotted on an échelle diagram this will leave three ridges; the two even ridges close together and the odd ridge further away. As discussed below in some situations the two even ridges can become blurred and appear to be a single ridge making identification challenging.

How clearly a frequency can be seen is dependent on its power (how strong the signal is relative to background noise) and its line width. The line width characterises the width of a peak in frequency when the data are plotted as a power spectrum. Although in some cases a wider peak may be easier to see, a large line width can reduce the frequency spacing between peaks to such an extent that two peaks will merge, creating what appears to be one peak. The width of a peak can arise from a number of different processes. On a

fundamental level any peak will have a width arising from the length of the observation. For solar-like stars most broadening arises due to properties of the star. If the oscillations within a star are heavily damped then the oscillations will have large line widths.

F-type main-sequence and subgiant stars are examples of where only two ridges can be clearly observed due to heavily damped oscillations, making mode identification challenging. F-type stars are hotter than the Sun, and show solar-like oscillations. Their higher temperature and fast rotation cause large line widths and significant rotational splitting. HD49933 is one example of an F-type star observed by the CoRoT spacecraft where mode identification has been difficult (for example, Appourchaux et al., 2008; Gruberbauer et al., 2009). Figure 2.1 is a plot taken from Gruberbauer et al. (2009) showing the difficulty in identification that can arise for such stars.

The aim of the work discussed in this chapter is to find a means to accurately identify the angular degree (ℓ) in problem stars. This method should enable us to produce a repeatable method that can be used on a number of stars without having to adapt the method for each case. Testing using stellar models enables us to verify the algorithm on a large number of different types of stars and to help us to establish how robust it is with different stellar properties. The methods discussed use scaling factors to enable comparisons of stars. The first uses a multiplicative scaling factor and has been called simply the *scaling method*. The second uses both a multiplicative factor and a linear offset so has been referred to as the *offset method*.

2.2 Scaling Method

Comparisons of stars can be used to gain information not only about differences between them but also extra knowledge on certain properties if they are known in one star and not the other. This idea of comparing stars to gain information is based on the theory of

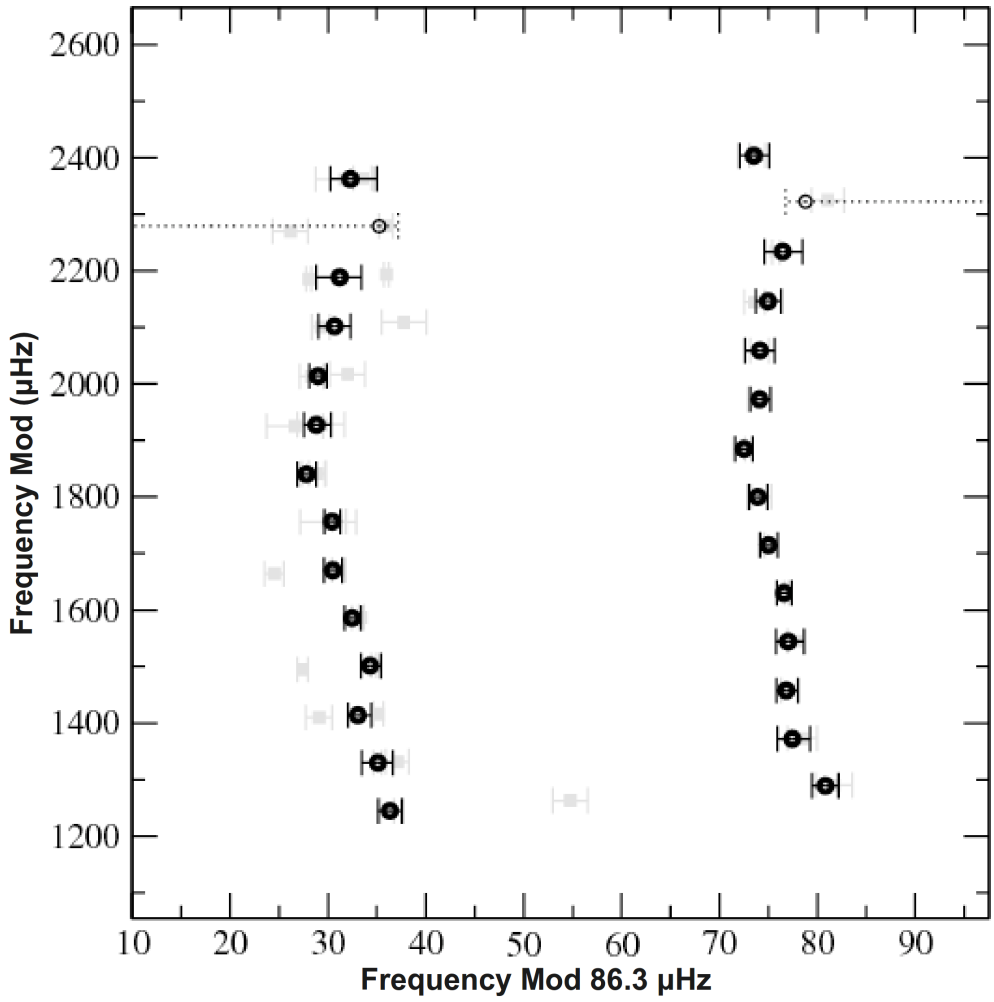

Figure 2.1: Échelle diagram of frequencies found in spectra of HD49933 from Gruberbauer et al. (2009), only two clear ridges are seen which makes ridge identification difficult.

homology. It uses the principle that properties within a star's interior obey scaling laws involving the star's fundamental properties, e.g. mass, radius, effective temperature. Stars of different mass, radius and luminosity which have the same relative mass distribution can be said to differ only in scale (Cox & Giuli, 1968). In this case we are assuming that a star's frequencies will scale with the large separation which in turn scales as $< \rho >^{1/2}$ i.e. $M^{1/2}R^{-3/2}$ where $< \rho >$ is the average density, M the mass and R is the radius of the star.

The first method of mode identification, which has been named the scaling method is introduced and described in this section. It uses the ideas behind an échelle plot as a way of comparing the seismic data received from two stars. An échelle plot can be used to split the frequencies observed from a star into rides of angular degree. Once the frequencies have been separated we minimise the frequency differences between each set of frequencies in an attempt to match ridges of the same angular degree. For this to be possible we need to be able to plot the frequencies of both stars on the same échelle diagram. The scale of the plot is determined by the star's large separation ($\Delta\nu$), as ν mod $\Delta\nu$ is used to line up the frequencies into ℓ ridges. If the $\Delta\nu$ is not a good match to the data then these ridges will not be seen. As two stars will have different properties it is necessary to adapt the one star to match the other. This can be achieved by multiplying the frequencies of one star by the ratio of their large separations, $r = \Delta\nu_A/\Delta\nu_B$, where A and B are used to denote the star with known identification and the star to be scaled, respectively. In practice the best scale factor, r, is not quite the ratio of the large separations but something close to it, as the stars are not quite homologous. This method could fail for cases where the two stars being compared have different surface terms. A surface term is used to account for discrepancies between modelled data and real data. This can have the effect of shifting the ridges on an échelle diagram meaning that if one star has a much larger surface term than the other, when both are plotted on the same échelle

diagram, the ridges will be offset. The discrepancies between models and real data occur because assumptions are required to model a star some of which, although accurate for the interior, fail at the surface. One important assumption is the use of the mixing length model of convection which does not work well in areas where convection is not efficient, like at the surface of a star. These types of problems lead to a frequency dependent error in the calculated frequencies called the surface term (Basu, Chaplin & Elsworth, 2010, and references therein). If this term is significantly different in the two stars being compared it could cause the method to mis-identify the angular degree of a mode. These problems will not appear when testing the method with model data. Testing this method will still provide information on the validity of methods using such scaling comparison techniques. Subsequent methods explored in this chapter attempt to remove the surface term problem.

The method described above has been used by Bedding & Kjeldsen (2010). They tested the method on three CoRoT F-type stars with ambiguous identifications and have showed that the method is able to successfully match ridges of different angular degree.

We assume that for stars where this method is needed only a combined ℓ=0, 2 and ℓ=1 ridges will be seen. For simplicity the ℓ=0, 2 ridges will subsequently be denoted by ℓ=0. If we have two ridges for each star and know the identification of one set of ridges but not the other then there are two ways that the ridges can be matched, with ℓ=0 of one star by ℓ=0 of the other, or mis-matched so ℓ=0 of one is by ℓ=1 of the other. The aim of this investigation is to find out how often the ridges of the same degree lie closer to each other than those of different degree. To test this we find which ridges are closest by using a sum that adds the differences between the sets of frequencies. The smaller the values of the sum the closer the ridges must be, so the better the match. Two different sums can be created, one comparing correctly matched frequencies and one comparing

mis-matched frequencies. These are shown in Equations 2.1 and 2.2 respectively.

$$S_{00,11} = \left[\sum_{n_{\rm low}}^{n_{\rm high}} (r v_{(\mathrm{B,n},\ell=0)} - v_{(\mathrm{A,n},\ell=0)})^2 + \sum_{n_{\rm low}}^{n_{\rm high}} (r v_{(\mathrm{B,n},\ell=1)} - v_{(\mathrm{A,n},\ell=1)})^2 \right] / n_{\rm ord}. \quad (2.1)$$

$$S_{01,10} = \left[\sum_{n_{\rm low}}^{n_{\rm high}} (r v_{(\mathrm{B,n},\ell=0)} - v_{(\mathrm{A,n},\ell=1)})^2 + \sum_{n_{\rm low}}^{n_{\rm high}} (r v_{(\mathrm{B,n},\ell=1)} - v_{(\mathrm{A,n},\ell=0)})^2 \right] / n_{\rm ord}, \quad (2.2)$$

Here ν_A denotes the frequencies of one star and ν_B the frequencies of the other and $n_{\rm ord}$ is the number of radial orders that would be observed through observations of such a star. Before the comparison can take place the frequencies from one star need to be scaled by r so the two stars appear to have the same large separation (hence the use of r in the above equations).

The individual frequencies are denoted by the star they are from (A or B), their angular degree (0 or 1) and their radial order, n. The radial order denotes the number of nodes the mode has within the star. This can also be challenging to identify accurately in observational data so suggests a possible problem with the method as the method assumes we are comparing frequencies with the same radial order. One solution to this problem is explored in Section 2.4. To test how well the method works here for identifying angular degree we will first use model data where the radial order of each frequency is assumed to be known.

From Equations 2.1 and 2.2 we can calculate the root mean square (RMS) residuals. We use the RMS as a means to identify how well the sum represents the data:

$$\sigma_{00,11} = \sqrt{\min(S_{00,11})}, \quad (2.3)$$

$$\sigma_{01,10} = \sqrt{\min(S_{01,10})}. \quad (2.4)$$

2.2.1 Testing the Method

In order to test the scaling method introduced above we use model frequencies. This gives the advantage of knowing what mode each of the frequencies correspond to, so we can check if the method gives the correct results. In this case low degree p-mode frequencies from a grid of models were used from the Yale-Yonsei isochrones (Demarque et al., 2004) which span a range of different evolutionary states. For this study we will be using the modes from solar-like stars. Figure 2.2 shows the complete set of models and the subset used in this study.

These models provide all the frequencies likely to be produced by a star. In reality the number of these frequencies with a large enough amplitude to be observed will be lower. The number of frequencies observed is proportional to the position of a star's maximum amplitude, $\nu_{\rm max}$. This can be estimated from a star's mass, M, radius, R, and effective temperature, T, by comparison to the Sun (Kjeldsen & Bedding, 1995; Brown et al., 1991), by using

$$\nu_{\rm max} = 3100 \left(\frac{M/M_{\odot}}{(R/R_{\odot})^2 \sqrt{(T/T_{\odot})}} \right) Hz. \tag{2.5}$$

To reduce the number of frequencies provided by the models to a number we can expect to observe we scale the number of observed frequencies against the number expected from a solar-like star,

$$n_{\rm ord} = 10 \frac{\nu_{\rm max}}{\nu_{\rm max\odot}} \tag{2.6}$$

where $\nu_{\rm max\odot}$ is the position of the Sun's maximum amplitude, ($\sim$3100μHz).

To perform the tests the models were ordered by either $\nu_{\rm max}$, $\Delta\nu$ or $T_{\rm eff}$. Here $\Delta\nu$ is the large separation and $T_{\rm eff}$ is the effective temperature. This ordering is an attempt to ensure that the stars being compared were similar. Once this list has been made pairs of stars were taken in turn and the method applied.

Figure 2.3 shows the results when this method is applied to the model data. We see

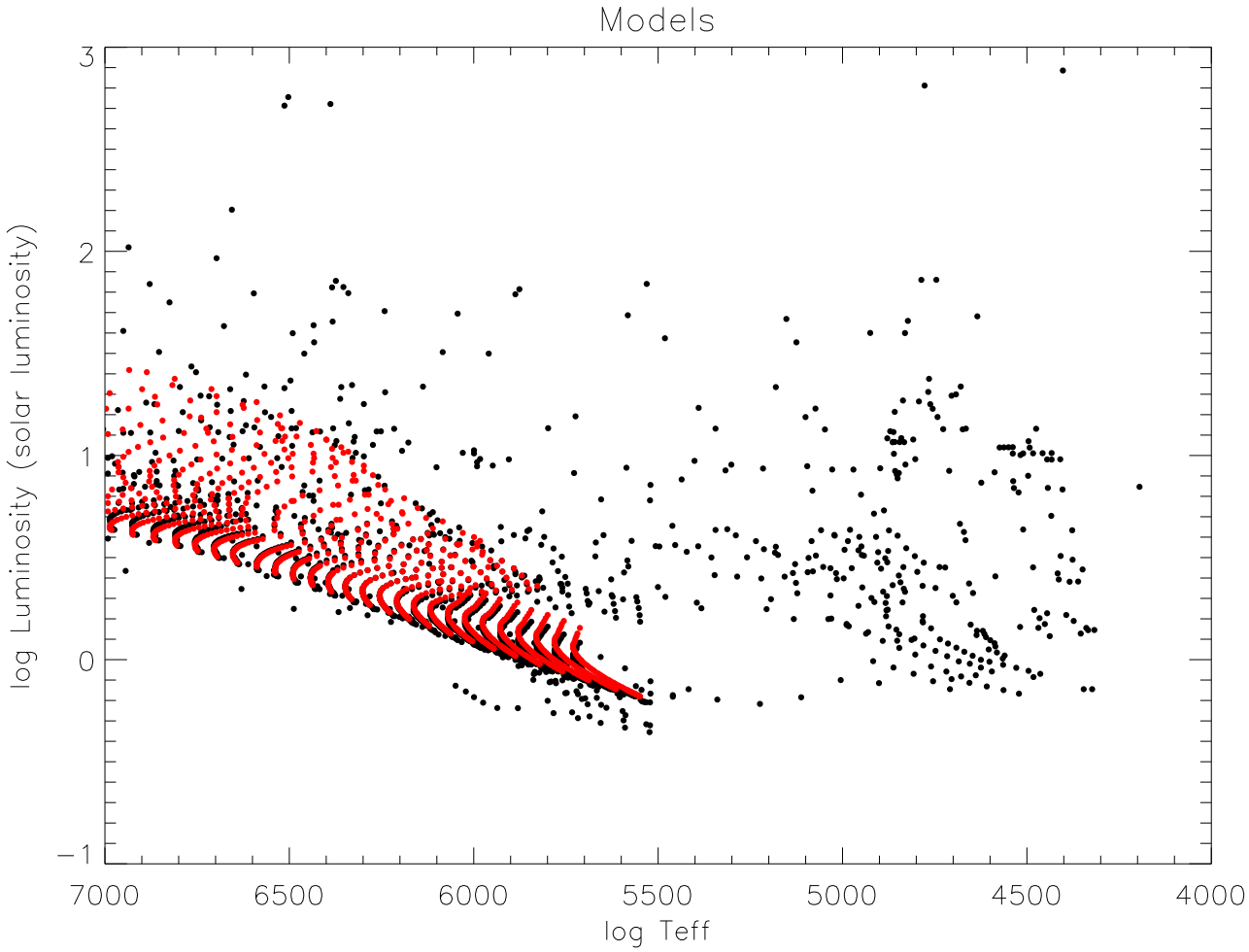

Figure 2.2: Hertzsprung-Russell diagram of model stars used to test ℓ identification methods. Black points show the positions of all modelled stars, red the positions of those used in this study. The stars chosen for this study are all main sequence stars with solar-like oscillations.

that the RMS for the majority of pairs is lower when the frequencies are matched correctly (black points). This method correctly identifies 1003 out of the 1005 model pairs tested, 99.8%.

This method is very successful for model data, however, as described earlier there is some doubt as to how well it will work for real stars as models do not represent the surface of a star accurately. If this term is significantly different in the two stars being compared it could cause the method to mis-identify the angular degree of a mode. These problems will not appear when testing the method with this model data.

2.3 Offset Method

The next step is to attempt to find a method that is not dependent on the effects of the surface term. A method that promises this uses the asymptotic relation (Hekker et al., 2011; Tassoul, 1980), which is shown in Equation 2.7, as a model of the expected frequencies. This holds reasonably well for the main-sequence solar-type stars used in this investigation:

$$\nu_{n,l} = \Delta\nu(n + l/2 + \epsilon) - Dl(l + 1). \tag{2.7}$$

Here D is sensitive to the gradient of the sound speed in the deep interior (for a solar-type star this will be a small fraction of $\Delta\nu$) and ϵ depends on the boundary conditions of the models (particularly those at the surface). For real stars this factor would also contain a contribution from non-adiabatic effects. This asymptotic relation can be used to express the frequencies of the two stars to be compared, i.e.

$$\nu_{A,n,l} = \Delta\nu_A(n + l/2 + \epsilon_A) - D_A l(l + 1), \tag{2.8}$$

$$\nu_{B,n,l} = \Delta\nu_B(n + l/2 + \epsilon_B) - D_B l(l + 1). \tag{2.9}$$

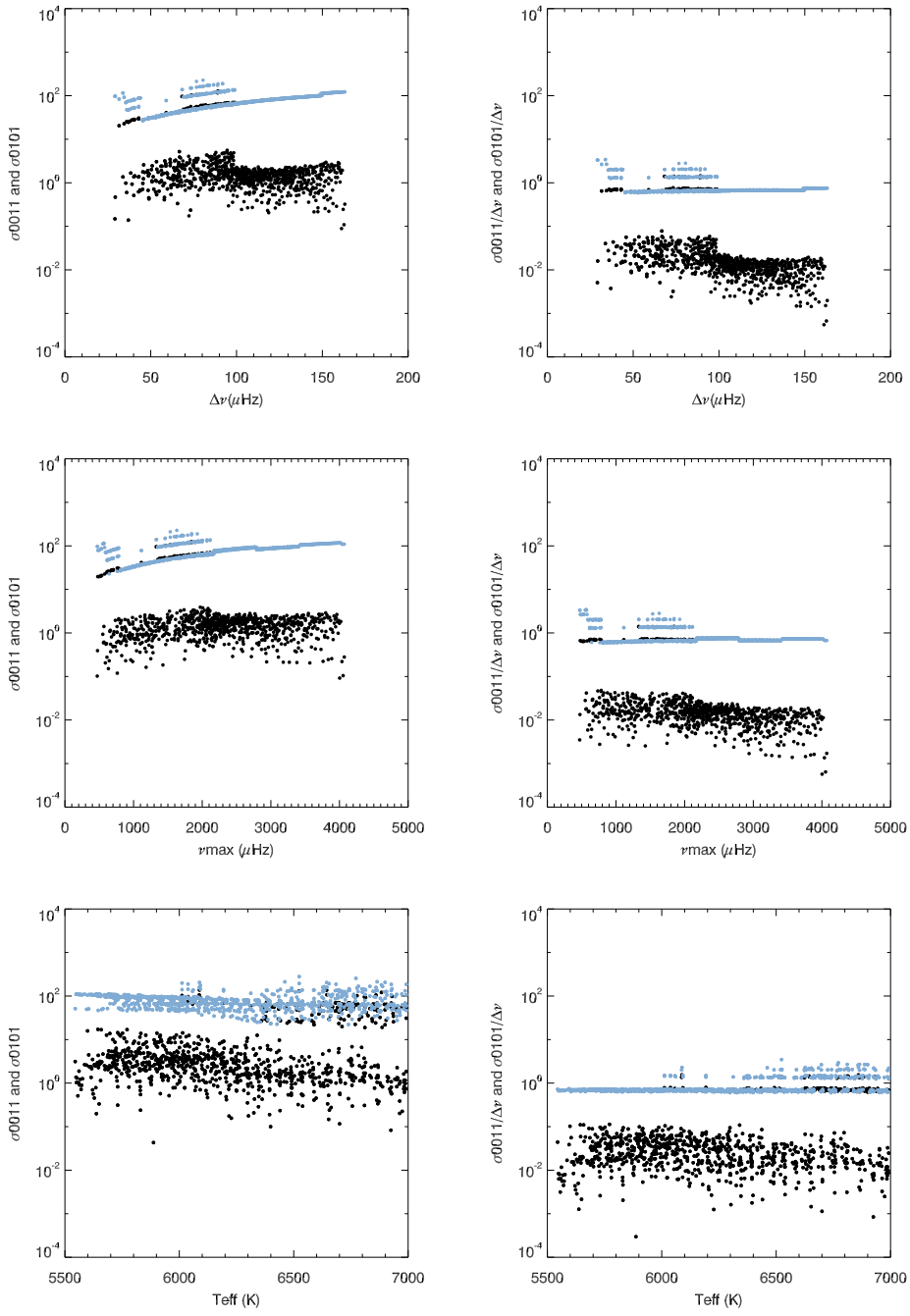

Figure 2.3: Plot showing the results of the scaling method when applied to model data. The blue points show stars where the frequencies are incorrectly matched and the black points where they are correctly matched. All plots show that the RMS, for the majority of pairs is smaller when modes are correctly matched. The top panels show the results when the models are ordered by $\Delta\nu$ the central by $\nu_{\rm max}$ and the bottom panels by $T_{\rm eff}$.

Before a comparison can be made the frequencies from star B need to be scaled to give star B the same large separation as star A. This is achieved by multiplying the frequencies of star B by the ratio of the large separations ($r = \Delta\nu_A/\Delta\nu_B$) as in the previous scaling method, giving:

$$r\nu_{B,n,l} = \Delta\nu_A(n + l/2 + \epsilon_B) - rD_B l(l+1). \tag{2.10}$$

If we now split these frequencies into contributions from their separate angular degrees we obtain four sets of frequencies, $\nu_{A,n,0}$, $r\nu_{B,n,0}$, $\nu_{A,n,1}$ and $r\nu_{B,n,1}$. From these we can find the four possible frequencies differences:

$$\nu_{A,n,0} - r\nu_{B,n,0} = \Delta\nu_A(\epsilon_A - \epsilon_B), \tag{2.11}$$

$$\nu_{A,n,1} - r\nu_{B,n,1} = \Delta\nu_A(\epsilon_A - \epsilon_B) + 2rD_B - 2D_A, \tag{2.12}$$

$$\nu_{A,n,0} - r\nu_{B,n,1} = \Delta\nu_A(\epsilon_A - \epsilon_B) + 2rD_B - \Delta\nu/2, \tag{2.13}$$

$$\nu_{A,n,1} - r\nu_{B,n,0} = \Delta\nu_A(\epsilon_A - \epsilon_B) - 2D_A + \Delta\nu/2. \tag{2.14}$$

Equation 2.11 shows the difference between frequencies of ℓ=0 for both stars as given by the asymptotic relation. Equation 2.12 shows this difference when ℓ=1 for both stars are compared. The differences obtained when ℓ=0 of one star is matched with ℓ=1 of the other are shown in Equations 2.13 and 2.14.

If $\nu_{A,n,0}$ is plotted against $\nu_{B,n,0}$, as seen in Figure 2.4, then the resulting graph will be a straight line of the form $y = mx + C$ where the gradient, m, is the scale factor, r and the offset, C, is different between the two sets of frequencies. This process can then be repeated for each of the four frequency differences. The offsets from the correctly matched frequency differences (Equations 2.11 and 2.12) lie much closer together than when the modes are mis-matched. More precisely, they show that the well matched modes have offsets that agree to within a small fraction of $\Delta\nu$ and all the other combinations differ from each other by either approximately $\Delta\nu/2$ or $\Delta\nu$. The term $\Delta\nu_A(\epsilon_A - \epsilon_B)$ holds the

information on the surface term of the stars. This is common to all four differences so will not change the relation between the four offsets, removing the methods dependence on the surface term as ϵ_A and ϵ_B are no longer required to be similar. This term will however still have an effect when plotting the offset values by moving all four of them away from the expected values shown below in Equations 2.15-2.18.

$$C_{0,0} = \Delta\nu_A(\epsilon_A - \epsilon_B), \tag{2.15}$$

$$C_{1,1} = \Delta\nu_A(\epsilon_A - \epsilon_B) + 2rD_B - 2D_A, \tag{2.16}$$

$$C_{0,1} = \Delta\nu_A(\epsilon_A - \epsilon_B) + 2rD_B - \Delta\nu/2, \tag{2.17}$$

$$C_{1,0} = \Delta\nu_A(\epsilon_A - \epsilon_B) - 2D_A + \Delta\nu/2. \tag{2.18}$$

The offsets can be calculated by minimising the following sum:

$$S_{l_A,l_B} = \left[\frac{1}{n_{\rm ord}}\sum_n (\nu_{(A,n,lA)} - rv_{(B,n,lB)} - C_{(lA,lB)})^2\right]^{\frac{1}{2}}. \tag{2.19}$$

This sum looks for the offset which minimises the differences between the two sets of frequencies. This is similar to the method used in the scaling method (Section 2.2.1) where the differences were minimised using the scale factor, r. Here we are effectively adding a second scaling factor, C. On an échelle plot the two scaling factors work together to shift the ridges of star B across and straighten them. Figure 2.5 explains this process, with frequencies created using the asymptotic relation with large separations of 70 and 72 μHz. This creates idealised frequencies. In reality and when more realistic models are used the ridges can be curved and even star A's ridges may not be perfectly vertical. The black points show the frequencies of star A, the grey points the unscaled frequencies of star B. The green points are the frequencies of star B scaled by r. This brings the large separation of star B in line with star A making the star B's ridges more vertical. Finally,

the blue points are the frequencies of star B scaled by r with an extra offset added. This moves the ridges along the plot to line up with those of star A. The optimum offset, C, could have any value in the range from $-\Delta\nu$ to $\Delta\nu$, depending on the surface term of the star.

This method has been tested on the same models as the previous method, which gives a range of stars with a variety of properties. To see how many pairs of stars this method correctly identifies the angular degree for, we can plot the values of C for each pair of stars against the $\Delta\nu$, $\nu_{\rm max}$ or $T_{\rm eff}$ of the comparison star. The offset values for each pair of stars will be very different and dependent on the values of $\Delta\nu$ and the factor $(\epsilon_A - \epsilon_B)$. These factors can be normalised by dividing each offset by the star's $\Delta\nu$ and removing the average of the four offsets for each star from each offset. If the method has succeeded it will show that the well matched frequencies give smaller offsets, with the other offsets multiples of $0.5\Delta\nu$ away.

The left hand images of Figure 2.6 show the offset divided by the large separation and shows the large scatter which arises from $(\epsilon_A - \epsilon_B)$ being different for each pair of stars. This effect has then been removed by subtracting the average. This is shown on the right half of Figure 2.6 and clearly shows that the offsets when modes are correctly matched (red and blue) are closer together than those which are matched incorrectly (black and grey). This seems to be the same regardless of how the stars are sorted, though the structure of the results is different when sorted by $T_{\rm eff}$. There are pairs included in this sample where the sums minimise in places other than where expected from the method. In Figure 2.6 the top graph on the right hand side shows the offset plotted against $\Delta\nu$. The pairs where the method appears to fail are for stars with a large separation between 70 and 110 μHz. To calculate the number of pairs for which the method obtains the correct identification we looked at the differences between the offset calculated for each pair of stars. Where the method has plotted a correct identification the gap between the

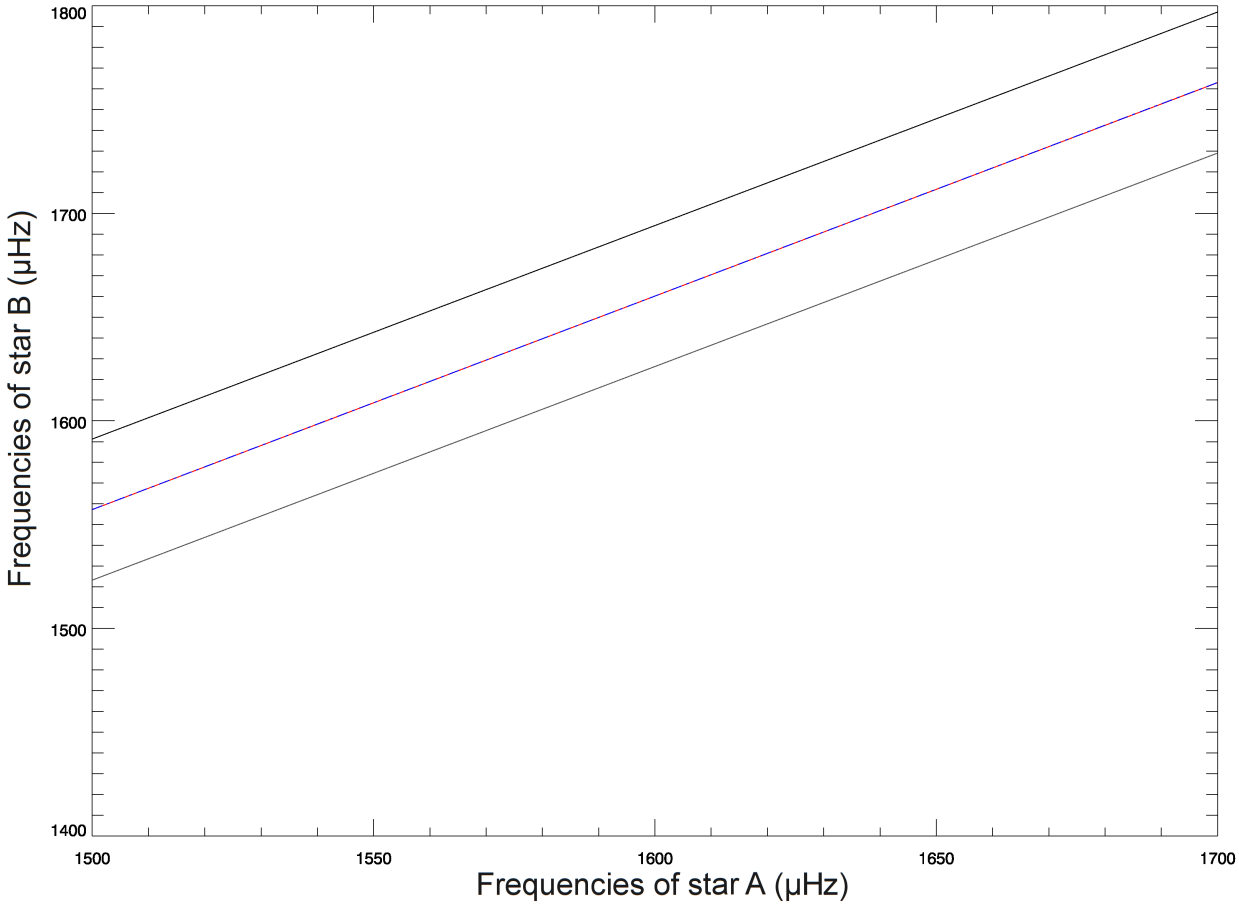

Figure 2.4: This figure shows the frequencies of one star plotted against those of another after they have been split into modes of 0 or 1. The red and blue lines show the position of the frequencies where the same orders have been plotted against each other. The grey and black lines show the positions when $\ell = 0$ is plotted against $\ell = 1$ and vice versa. Here we can see that the well matched cases are closer together than any other combination.

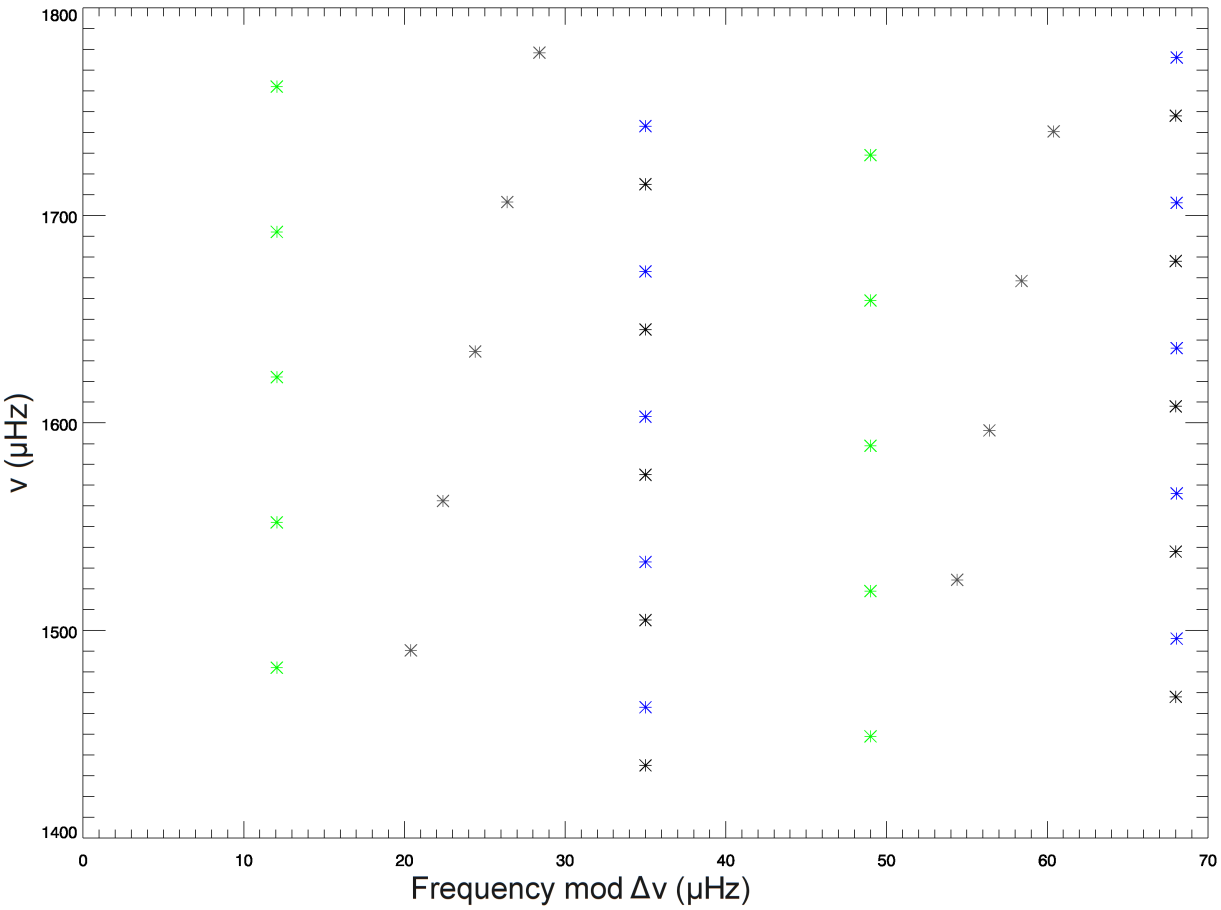

Figure 2.5: This figure uses frequencies created from the asymptotic relation with large separations of 70 and 72 μHz. The black points show the frequencies of star A, the grey points the unscaled frequencies of star B. The green points are the frequencies of star B scaled by r. This has the effect of straightening the ridges. Finally the blue points are the frequencies of star B scaled by r with an extra offset added, this moves the ridges along the plot to line up with those of star A.

Ordered by	Number of working pairs
$\nu_{\rm max}$	925
$\Delta\nu$	927
$T_{\rm eff}$	845

Table 2.1: The number of pairs for which the offset method works when the stars are ordered by $\nu_{\rm max}$, $\Delta\nu$ and $T_{\rm eff}$. In all cases a total of 1005 pairs have been tested.

offsets where ℓ=0 is matched with ℓ=0 and $\ell = 1$ is matched with $\ell = 1$ will be closest and have the smallest difference. Using this test we can see how many pairs the method works for, and these results are shown in Table 2.1. The method works in 92% of cases when the stars are ordered by $\nu_{\rm max}$ and $\Delta\nu$ and 84% when ordered by $T_{\rm eff}$. This is less effective than the scaling method but as it is not reliant on the surface terms of the two stars being the same it should be more successful when applied to real data.

2.4 Reduced Frequencies

The methods discussed so far in this chapter require accurate knowledge of the radial order, n. This information allows us to match frequencies on a mode-by-mode n-by-n basis. This is a useful first test but the radial order can be as difficult to identify as the angular degree. In an attempt to combat this issue the offset method has been adapted so that the matches are made by frequency rather than n.

In order to use frequency rather than n to make these matches we need to do two things; find/create another variable to perform the tests on and interpolate the second star's frequencies so values of this new variable are known at the same frequency as the first. The new variable we introduce is a reduced frequency. The frequencies can be converted into a set of reduced frequencies according to:

$$\xi_{A,n,l} = \nu_{A,n,l} \bmod \Delta\nu_A, \tag{2.20}$$

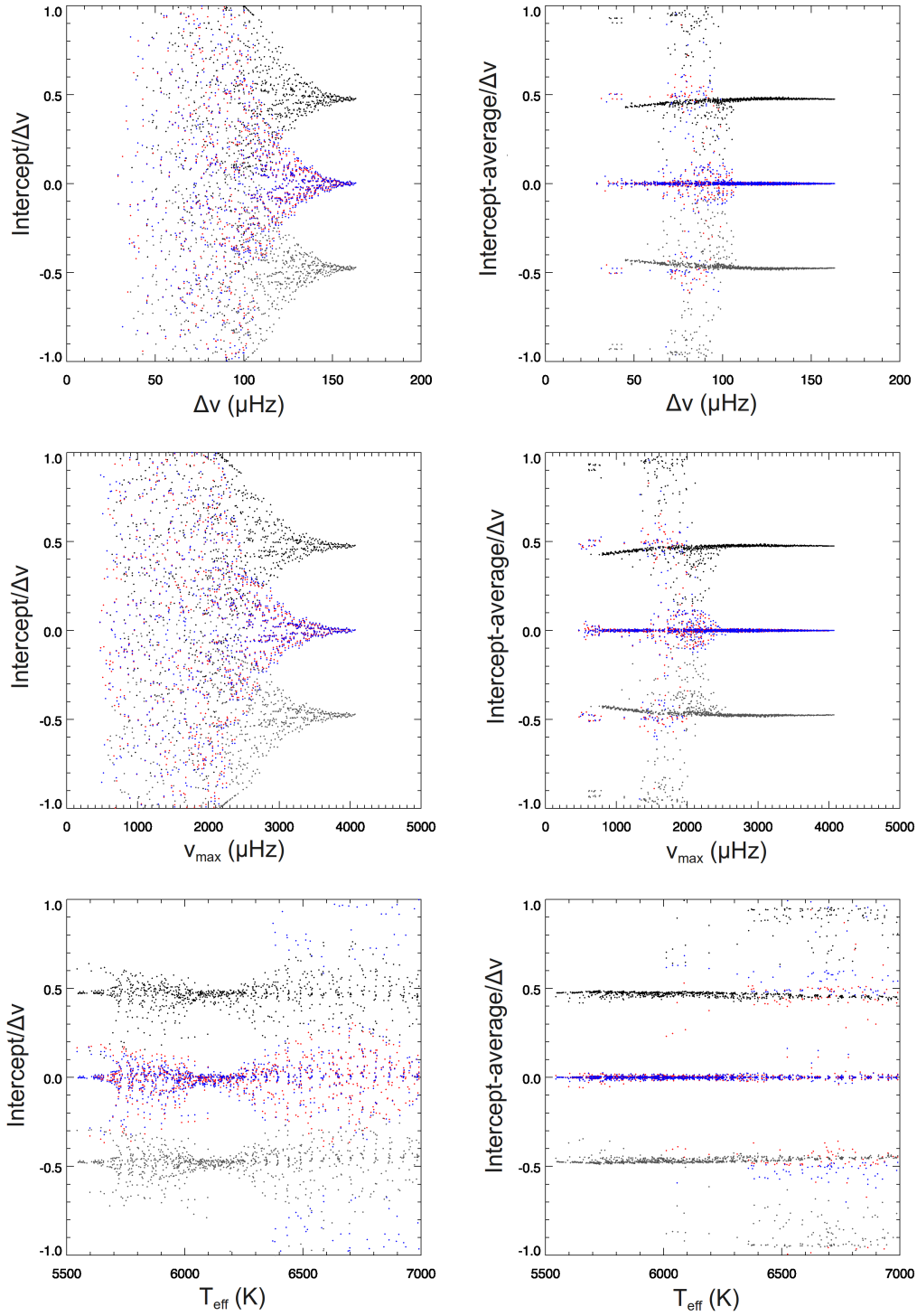

Figure 2.6: Results of the offset method applied to model data. The top panels show the results when the models are ordered by $\Delta\nu$ the central by $\nu_{\rm max}$ and the bottom by $T_{\rm eff}$. The left hand plots show a large scatter which arises from $(\epsilon_A - \epsilon_B)$ being different for each pair of stars. This has been removed from the right hand plots by subtracting the average.

where $\Delta\nu_A$ is the average large separation of the first star. The frequencies of the second star need to be scaled by the ratio of the large separation, r, as in the scaling method this factor is used to make the large separation of the two stars comparable,

$$\xi_{B,n,l} = r\nu_{B,n,l} \bmod \Delta\nu_A. \tag{2.21}$$

This is the same quantity calculated for an échelle plot. Unfortunately, this does not always provide a continuous result, as the quantity can wrap around. Wrap around features are often seen in échelle plots as the ridges created from frequencies of the same degree are rarely perfectly vertical, so they will slant towards the edge of the plot, an example is shown in Figure 2.7. The ridge can then wrap around the plot and appear on the other side.

First we split the frequencies for each star into two groups corresponding to their angular degree. For star A we know the identification of each group for star B we assume an identification and use the method to determine if this is correct or incorrect. For each of star A's frequency groups we then take the frequency closet to $\nu_{\max}$, $\nu_{A,n_0,l}$, and calculate it's reduced frequency.

$$E_{A,l=0} = \nu_{A,n_0,l=0} \bmod \Delta\nu_A, \tag{2.22}$$

$$E_{A,l=1} = \nu_{A,n_0,l=1} \bmod \Delta\nu_A. \tag{2.23}$$

This is then used as the basis to calculate the rest of the reduced frequencies for this star:

$$\xi_{A,n,l=0} = E_{A,l=0} + (\nu_{A,n_A,l=0} - \nu_{A,n_0,l=0}) - (n_{A,l=0} - n_0)\Delta\nu_A, \tag{2.24}$$

$$\xi_{A,n,l=1} = E_{A,l=0} + (\nu_{A,n_A,l=1} - \nu_{A,n_0,l=1}) - (n_{A,l=1} - n_0)\Delta\nu_A. \tag{2.25}$$

This process can be repeated for the frequencies of the second star. Here we also

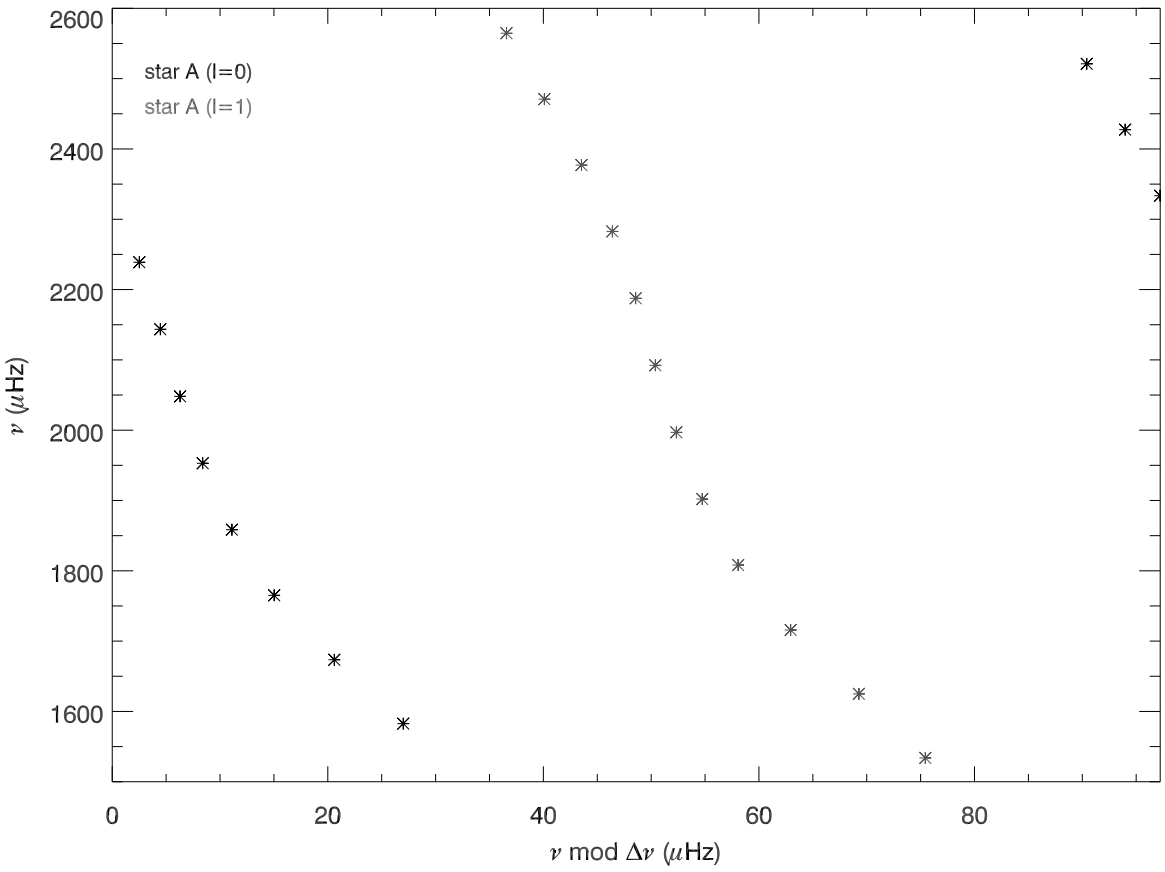

Figure 2.7: Example of an échelle diagram where a wrap around occurs. As one ridge reaches the edge of the plot it wraps around to appear on the other side.

include the two scale factors: r to make the large separations comparable and the offset, C, which is the variable we hope to use to obtain the identification. For any test value of C we obtain:

$$E_{B,l=0} = (r\nu_{B,n_0,l=0} - C_{l_A,l_B}) \mod \Delta\nu_A, \tag{2.26}$$

$$E_{B,l=1} = (r\nu_{B,n_0,l=1} - C_{l_A,l_B}) \mod \Delta\nu_A. \tag{2.27}$$

The optimum value of C will again be found by minimising the space between ridges, however, unlike before the offset will not be explicitly present in the sum but in the calculation of star B's reduced frequencies. The offset, C, is added to the original frequencies so it will follow the same rules set out in the original offset method,

$$\xi_{B,n,l=0} = E_{B,l=0} + (r\nu_{B,n_B,l=0} - \nu_{B,n_0,l=0}) - (n_{B,l=0} - n_0)\Delta\nu_A, \tag{2.28}$$

$$\xi_{B,n,l=1} = E_{B,l=1} + (r\nu_{B,n_B,l=1} - \nu_{B,n_0,l=1}) - (n_{B,l=0} - n_0)\Delta\nu_A. \tag{2.29}$$

The reduced frequencies can now be interpolated from $r\nu_B$ to ν_A to give ξ'_B. As in the original offset method we find the optimum values for C by minimising a sum:

$$S_{l,l'} = \left[\frac{1}{n_{\rm ord}} \sum_n \left(\xi_{A,n,l} - \xi'_{B,n,l}\right)^2\right]^{1/2}, \tag{2.30}$$

In order to minimise this sum we need to loop from the calculation of star B's reduced frequencies (Equations 2.26 and 2.27) to the calculation of the sum (Equation 2.30).

This method has been tested on the model data used in the previous tests, the results of which can be seen in Table 2.2. This shows that the method is not as effective as when the angular degree is known, and further investigation leads to wrap around effects being the main cause. Wrap arounds can still cause problems as although single ridges will not wrap around their overall position will. This is caused by the value of $E_{B,\ell}$

Ordered by	Number of working pairs
$\nu_{\max}$	887
$\Delta\nu$	900
$T_{\rm eff}$	855

Table 2.2: The number of pairs for which the offset method works when using the reduced frequencies. The stars are ordered by $\nu_{\max}$, $\Delta\nu$ and $T_{\rm eff}$. In all cases a total of 1005 pairs have been tested.

wrapping around as we run through test values of C. Such wrap around features can affect this method by causing the offsets to minimise twice at both the expected value and the expected value $\pm\Delta\nu$. The way the sums minimise is shown in Figure 2.8. This can then change the differences between the offsets causing mis-matched cases to appear closer than those which are well matched. The range of offset values searched is $-\Delta\nu$ to $\Delta\nu$, this range has been chosen to accommodate the range of offset values that arise from the factor $\Delta\nu_A(\epsilon_A - \epsilon_B)$. Ideally the range would cover only $\Delta\nu$ not $2\Delta\nu$. This smaller range would limit the number of times each sum can minimise to one, removing the issues caused by wrap around effects. However, the range $-0.5\Delta\nu$ to $0.5\Delta\nu$ will only include the four expected offsets when the factor $\Delta\nu_A(\epsilon_A - \epsilon_B)$ is zero (the two stars have the same surface term). When this is not the case this range will give a mixture of expected results and those caused by wrap around values. Figure 2.9 shows an example of where such sums minimise. The largest difference between offsets is no longer between the two mis-matched cases. The smallest difference is still between sums from the correctly matched cases.

The differences between offsets without any wrap around effects can be calculated from Equations 2.15 to 2.18 and expressed by,

$$C_{0,0} - C_{1,1} = 2D_A - 2rD_B, \tag{2.31}$$

$$C_{0,1} - C_{1,0} = 2rD_B + 2D_A - \Delta\nu. \tag{2.32}$$

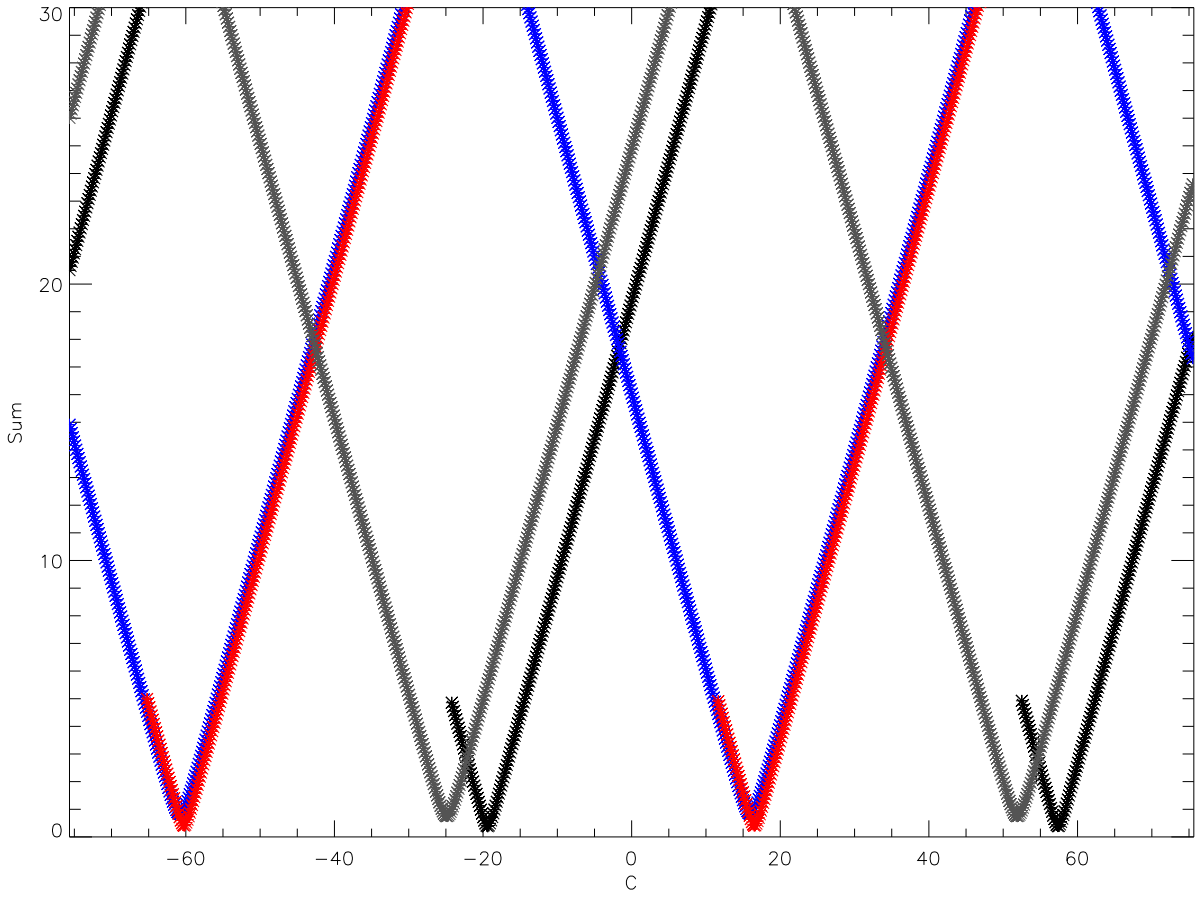

Figure 2.8: An example of the way the four sums minimise for a pair of stars. Red and blue mark the sums from the well matched cases and black and grey the mis-matched cases, the range shown is from $-\Delta\nu$ to $\Delta\nu$ so each sum is able to minimise twice.

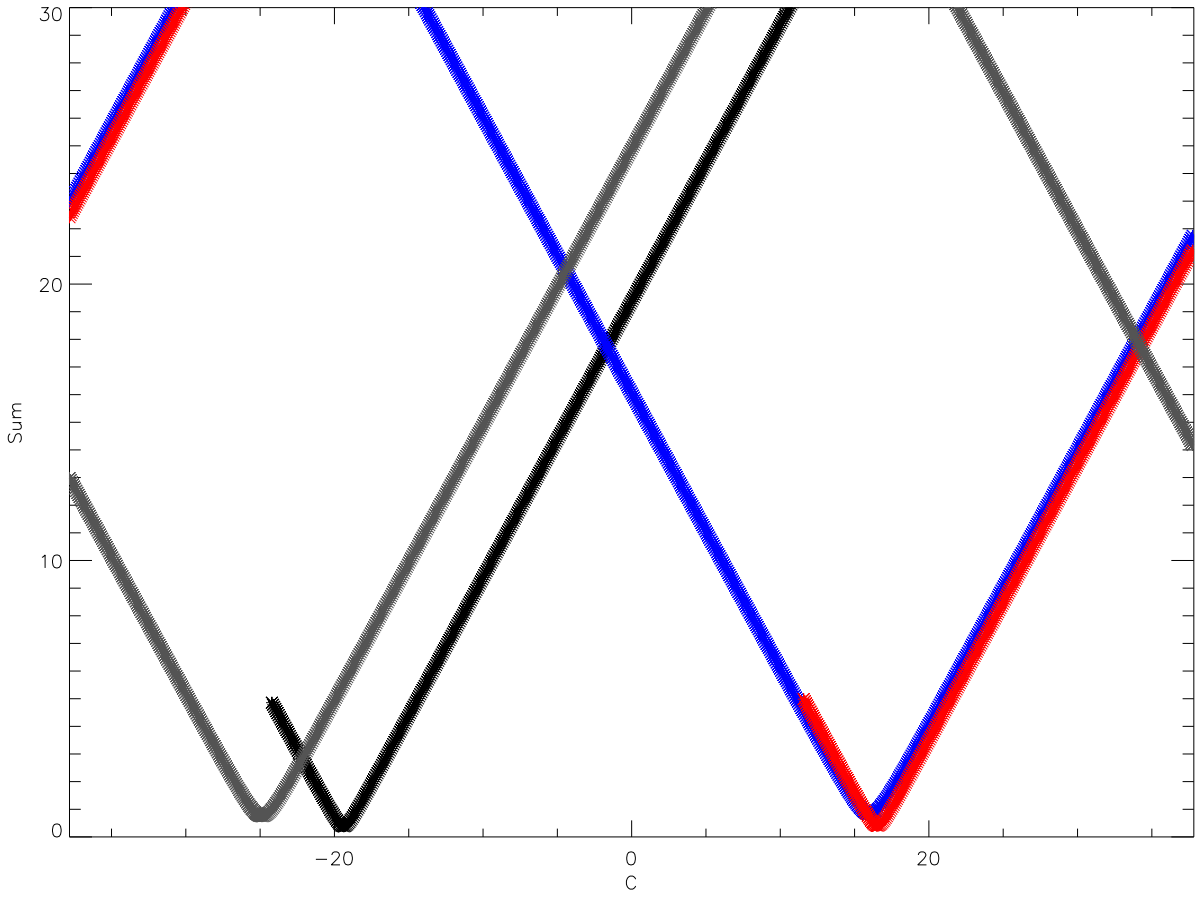

Figure 2.9: When the range is reduced to $-1/2\ \Delta\nu$ to $1/2\ \Delta\nu$ the sum can only minimise once. The largest distance is no longer between the two mis-matched cases (shown in black and grey). The smallest difference is still between the two well matched cases.

Ordered by	Number of working pairs
$\nu_{\max}$	1003
$\Delta\nu$	1003
$T_{\rm eff}$	976

Table 2.3: The number of pairs for which the adapted offset method works when the stars are ordered by $\nu_{\max}$, $\Delta\nu$ and $T_{\rm eff}$. In all cases a total of 1005 pairs have been tested.

Equation 2.31 shows the smallest difference which arises from the offsets of well matched frequencies and Equation 2.32 shows the largest difference from the mis-matched offsets. These will change if one of the offsets is affected by a wrap around effect. This wrap around is effectively like adding $\Delta\nu$ to one of the offsets. If we assume the offset $C_{0,1}$ was affected by the wrap around then the two differences become:

$$C_{0,0} - C_{1,1} = 2rD_B - 2D_A, \tag{2.33}$$

$$C_{0,1} - C_{1,0} = 2rD_B + 2D_A. \tag{2.34}$$

This dramatically reduces the difference between the two differences but as D_A and D_B should be similar for similar stars the difference between the two should be about $4D$.

This points towards a method that will correctly identify the angular degree from offsets found between $-0.5\Delta\nu$ and $0.5\Delta\nu$ by assuming that the distance between offsets created from the two well matched cases will be the smallest between any two offset values. The difference between the two offsets that arise from the mis-matched frequencies will only be the largest in particular cases, where the two stars have the same surface term. The results from testing this can be seen in Table 2.3. When ordered by $\nu_{\max}$ and $\Delta\nu$ the method works in 99.8% of cases and when by ordered by $T_{\rm eff}$ works in 97.1% of the cases tested. This suggests that ordering by $T_{\rm eff}$ is not as effective in ensuring that the stars being compared are similar and homologous as ordering by $\nu_{\max}$ and $\Delta\nu$.

Scaling	Original offset method	Adapted offset method
10	864	1003
5	857	950
3	836	898

Table 2.4: The number of pairs of stars where the method works with different number of observed frequencies, out of a sample of 1005 pairs. In all these cases the stars were first ordered by $\nu_{\max}$.

2.4.1 Number of Observed Frequencies

Throughout these tests we have assumed that a typical solar-like star will exhibit 10 modes of oscillation. This is controlled by scaling Equation 2.6. Here we reduce this number to see how well the method fares in less ideal situations. Table 2.4 shows the results of this method when the typical number is reduced to 5 and to 3. The adapted offset method shows resilience to this reduction with the changes having a small effect on the number of pairs for which a correct identification is found. The reduction appears to have even less effect on the original method as a smaller reduction is seen however as it begins with a lower success rate even with the scaling factor set to 3 the adapted offset remains more successful.

2.4.2 Noise

The data used so far are clean model data. Real data has noise so to further test the method we add mock noise to the model data. Here we assume random Gaussian noise will be a good representation of the noise we estimate the frequencies will have. We apply noise of mean zero and an RMS of 0.5μHz and 1.0μHz. The addition of noise reduced the effectiveness of both the original and adapted offset methods. The adapted methods success rate is reduced to 96.9% for 1.0μHz. This is still more successful than the original offset method with no noise and means the method should work in 24 out of 25 cases. As we are dealing with fitted frequencies we would expect the error to be around 1.0μHz.

	Original offset method	Adapted offset method
no noise	864	1003
0.5μHz	859	994
1.0μHz	837	974

Table 2.5: The number of pairs of stars where the method works with offset methods 1 and 2 out of a sample of 1005 pairs. In all these cases the stars were first ordered by $\nu_{\max}$.

These results can be seen in Table 2.5. To further test the methods resilience to large noise levels, it's success has been tested up to a level of 2.5μHz at this level the success rate nears 75%. These results are seen in Figure 2.10.

2.5 Conclusion

The aim of this investigation has been to produce an automated pipeline that is able to distinguish between frequencies produced by modes of oscillations of angular degree $\ell = 0$ and angular degree $\ell = 1$. All the methods that have been tested use different scaling factors to enable the use of comparison techniques. The first method uses a multiplicative scale factor to force the two stars to have a comparable large separation. The idea behind this method is that once on the same échelle plot the ridges of the two stars will line up so that corresponding ridges are close together. When this method has been tested on model data this does appear to be the case 99.8% of the time but this method could have problems when applied to data from real stars. If the two stars have different surface terms then the ridges will not align as expected. To combat this an alternative method has also been explored which arises from the asymptotic relation. This method is less vulnerable to the effects of the surface term and while it shows some success, providing accurate identifications in up to 92% of cases, it still requires previous knowledge of the radial order of a mode. To remove this dependence an alternative offset method has been tested that uses a reduced frequency in place of the frequency directly observed in observation.

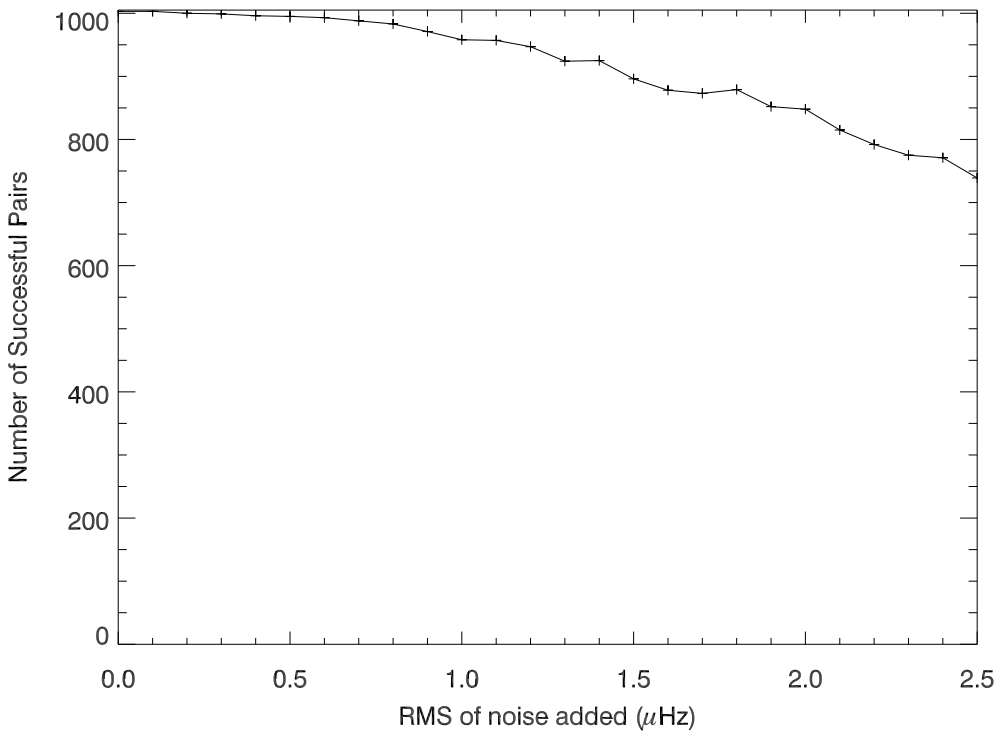

Figure 2.10: Plot showing the effect of adding noise to the model data when using the adapted offset method. The success rate decreases until it reaches 50% when the noise reaches 5μHz.

This enables the matches to be performed by frequency rather than radial order. When tested on model data this method does not appear to be as reliable as when knowledge of n is assumed. This appears to be caused by wrap around effects. To deal with this a slightly altered method which constrains the possible values of the offset has also been developed. When applied to model data this method shows promising results returning to the same levels of success as the original method (99.8%). This last method has also been tested for worse than expected observations (by reducing the number of frequencies used to perform the identification) and the effects of noise. The method remains reliable for both of these tests suggesting that it could prove to be useful when applied to data obtained from real stars.

Chapter 3

Changes Between Solar Cycles

3.1 Introduction

Solar activity has a great impact on life on Earth from effects on the climate to solar flares disrupting satellites. One goal of solar astronomy is to be able to predict how active the next solar cycle will be and when individual events such as solar flares will occur (Schatten et al., 1978; Hathaway et al., 1999; Pesnell, 2008, for example). In order to do this we need to know how changes within the Sun affect this activity. In this study we use helioseismic observations taken by the Birmingham Solar-Oscillations Network (BiSON) to see how the Sun has changed between solar cycle minima. The most recent minimum was much longer and quieter than had been expected from the activity levels of those before. Solar activity can be measured by a number of different indicators including Sunspot number. Figure 3.1 uses Sunspot numbers collected by SIDC (Solar Influences Data Analysis Centre) at the Royal Observatory of Belgium[1] to show how the most recent cycle compares to an average solar cycle. Sunspot numbers since 1949 have been split into 11 year sections and averaged together to give an idea of a normal cycle. Laid on top in blue are the Sunspot numbers for the last eleven years. The plot shows a minimum that reaches lower and lasts longer than the averaged data.

[1] `http://sidc.oma.be/`

The frequencies of p-mode oscillations are dependent on the internal structure of the star and so are expected to respond to changes within the Sun. The first evidence of such changes was seen between the years 1980 (close to solar maximum) and 1984 (close to solar minimum) by Woodard & Noyes (1985). They found a frequency shift of around 0.5 μHz. Since then other parameters have been found that also change with activity including the power of a mode, the damping rate and the peak asymmetry, (Chaplin et al., 2007; Komm et al., 2002; Salabert et al., 2003).

There also appears to be a frequency dependence to the way the frequencies shift with activity. Below about 4000 μHz frequencies are seen to increase with increasing activity. For modes around 3000 μHz the size of the shift is about 0.4 μHz (Woodard & Noyes, 1985; Salabert et al., 2003). This dependence suggests the perturbation responsible is close to the surface. The upper turning point of low-frequency modes lie deeper inside the Sun than those of high-frequency modes meaning high-frequency modes are more sensitive to surface perturbations.

From observations of medium ℓ frequency shifts it is possible to produce a map showing the strength of these frequency shifts as a function of latitude and time (Howe, Komm & Hill, 2002), like the example shown in Figure 3.2. This map shows similar features to the butterfly diagram (see Figure 1.9 in the introduction chapter) which shows spacial variations in the strength of the surface magnetic field over time. This shows a link between the frequency shift and the strength of the magnetic field. Various investigations have been made into the link between activity, frequency shifts and magnetic field strength. They have shown that the sizes of the low ℓ shifts scale better with activity proxies that have the same spherical harmonic projection as the modes (Chaplin et al., 2004; Jimenez-Reyes et al., 2004). Chaplin et al. (2004) have also shown that activity proxies with a good sensitivity to the effects of the weak-component of the magnetic flux (which is more widely distributed in latitude than the strong flux in the active regions) show a better

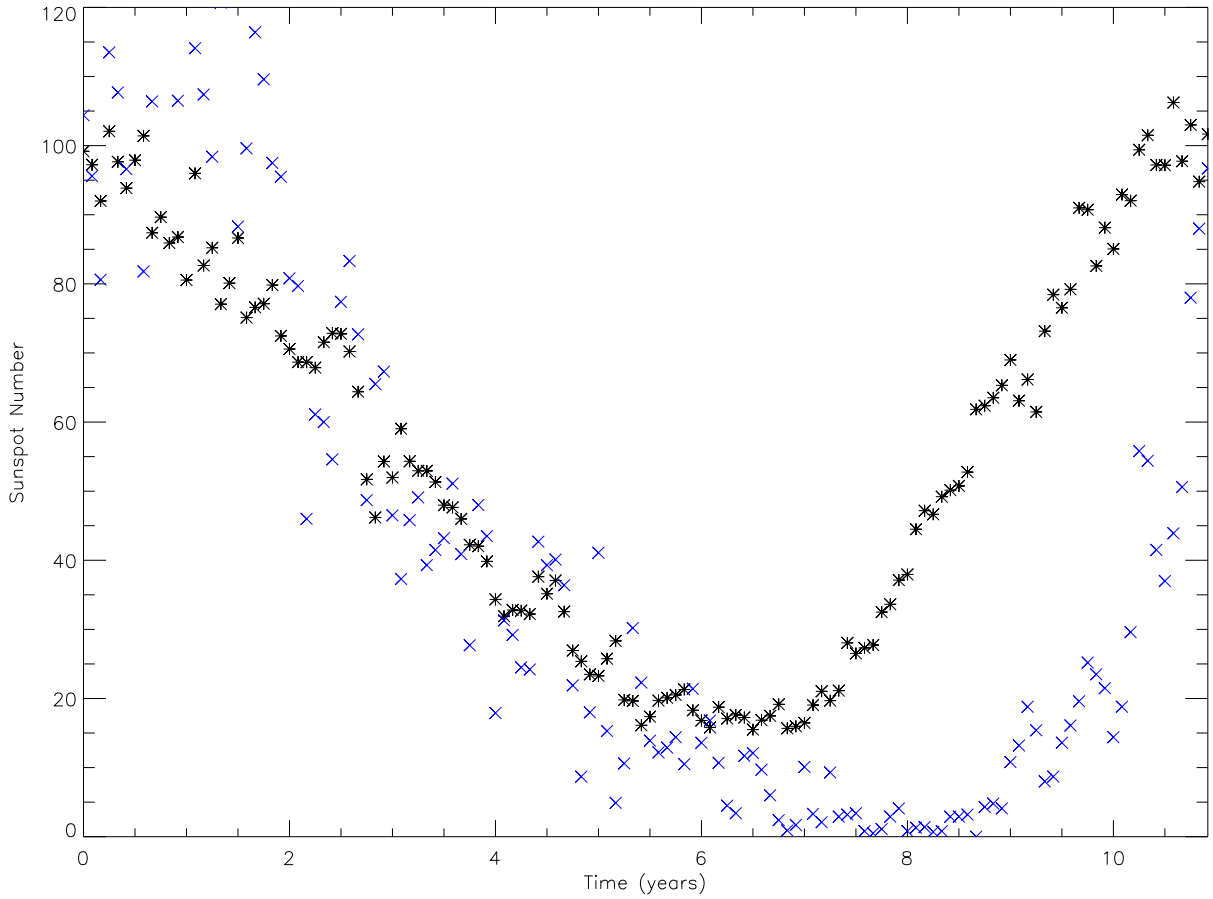

Figure 3.1: Data from SIDC at the Royal Observatory of Belgium used to show how the most recent cycle compares to an "average" solar cycle. Sunspot numbers since 1949 have been split into 11 year sections and averaged together to give an idea of a normal cycle, shown in black. Laid on top in blue crosses are the Sunspot numbers for the last eleven years, which shows a minimum that reaches lower and lasts longer than the averaged data.

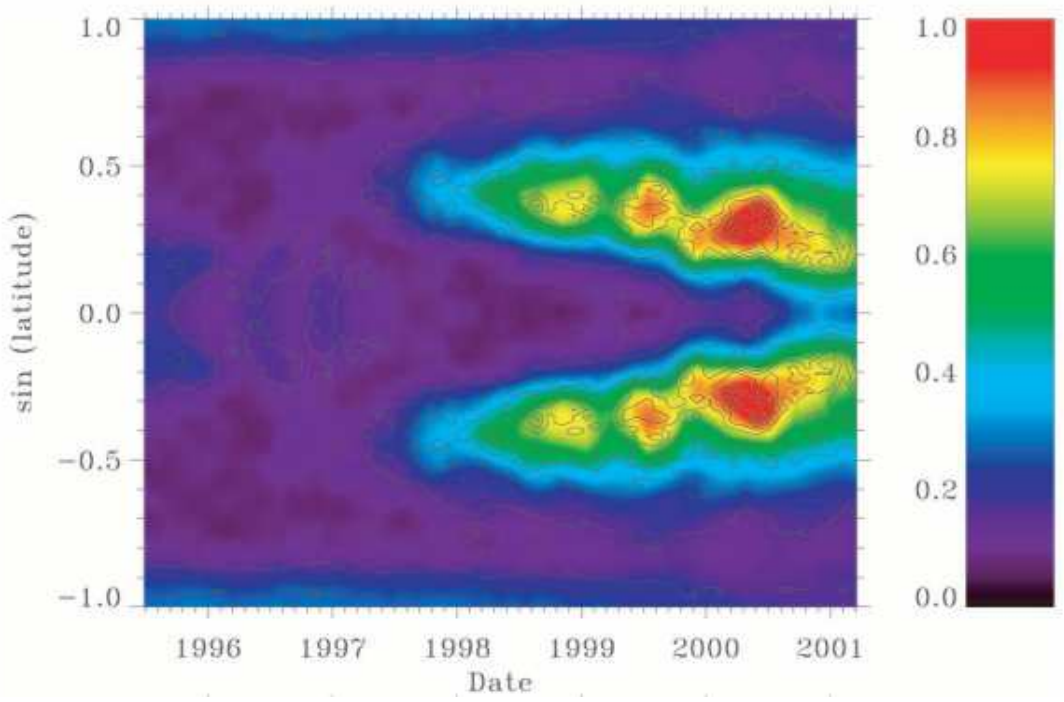

Figure 3.2: Mode frequency shifts as a function of latitude and time. Figure from Howe, Komm & Hill (2002).

correlation with the size of frequency shifts.

Examination of frequency shifts has also recently led Broomhall et al. (2009) to suggest the possible existence of a quasi-biennial modulation in the frequency of low-degree modes which is superimposed on top of the well established 11-year solar cycle, which has since been confirmed by further analysis (Fletcher et al., 2010).

The BiSON project makes Sun-as-a-star unresolved observations, and hence determines frequencies of low-degree modes ($\ell = 0$, 1, 2 and 3). We want to use these data to investigate changes in the internal structure of the Sun over 3 solar cycles. We analyse data collected during the minima before cycles 22, 23 and 24 (the current cycle). Two sample lengths are chosen, one year and two years, to see if length of sample effects the results. The one-year periods start in April 1986, November 1995 and May 2008 and the two-year periods start in October 1985, May 1995 and November 2007. These ranges can

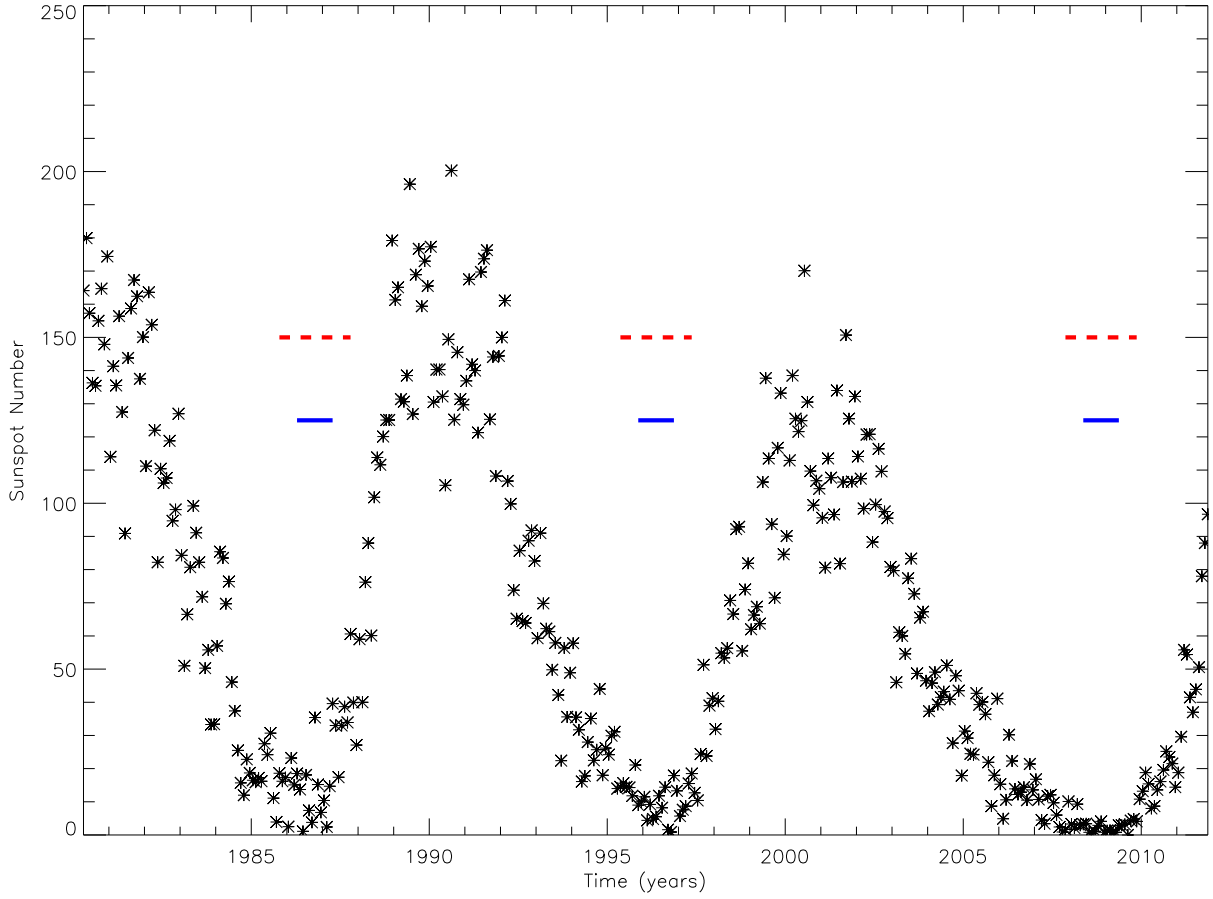

Figure 3.3: The Sunspot numbers recorded over the last 3 solar cycles are shown with indications of the sections of data used in this study. The dates for the one year data are shown in blue and the two year in red. Data from SIDC at the Royal Observatory of Belgium.

be seen in Figure 3.3 which shows the Sunspot number over the last three cycles. The one year data regions are marked by solid blue lines and the two year periods by dashed red.

3.2 Analysis

Initially we looked at changes in the asteroseismic quantities of the large and small separations. The large separation is the difference between frequencies of the same angular

degree and sequential radial orders (Equation 3.1):

$$\Delta\nu(\ell) = \nu_{(l,n+1)} - \nu_{(l,n)}. \tag{3.1}$$

The small separation is the difference between frequencies whose degrees differ by two and orders by ± 1 (Equation 3.2):

$$\delta\nu_{(l,l+2)} = \nu_{(l,n)} - \nu_{(l+2,n-1)}. \tag{3.2}$$

The comparisons for the two-year sets are shown in Figures 3.4 and 3.5. These show very small differences between the three minima, though differences in large separation for ℓ=3 do show some small differences which could indicate small scale changes in the solar interior. To test the significance of this we performed a Kolmogorov-Smirnov test (Kolmogorov, 1956). This showed the large separations to be very similar, with the largest differences shown between cycles 22 and 24 for ℓ=0 and ℓ=2. However, the probability of the two distributions being the same is around 50% meaning this is not significant. The larger errors seen in the data from cycle 22 make it hard to uncover any significant changes. If the same test is applied to the small separations they are also all shown to be similar.

The next step is to look at how the frequencies themselves have changed by calculating the differences in the solar oscillation frequencies between the three minima. The pairs of differences for the two- and one-year data sets are shown in Figures 3.6 and 3.7 respectively. These figures show that the differences are small but not completely random as they show a periodic variation with frequency. This suggests that the frequency differences arise from an abrupt change within the Sun. Such changes are known to create a characteristic periodic signature in frequency (Gough, 1990; Basu et al., 1993; Roxburgh & Vorontsov, 1994). The period of such a feature holds information on the location of the region of

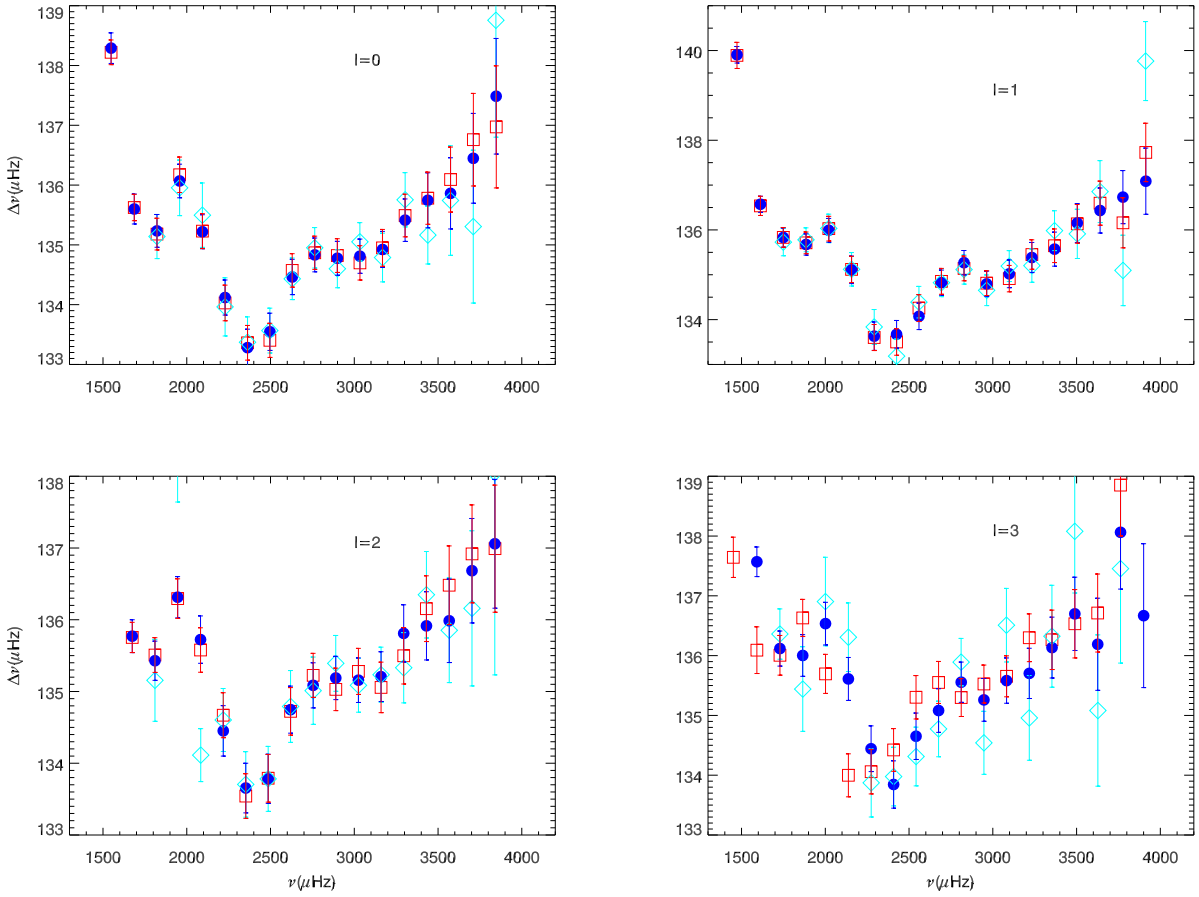

Figure 3.4: The large separations for each minima are shown. Cycle 22 is shown by the light blue diamonds, cycle 23 by the dark blue filled circles and cycle 24 by the red squares.

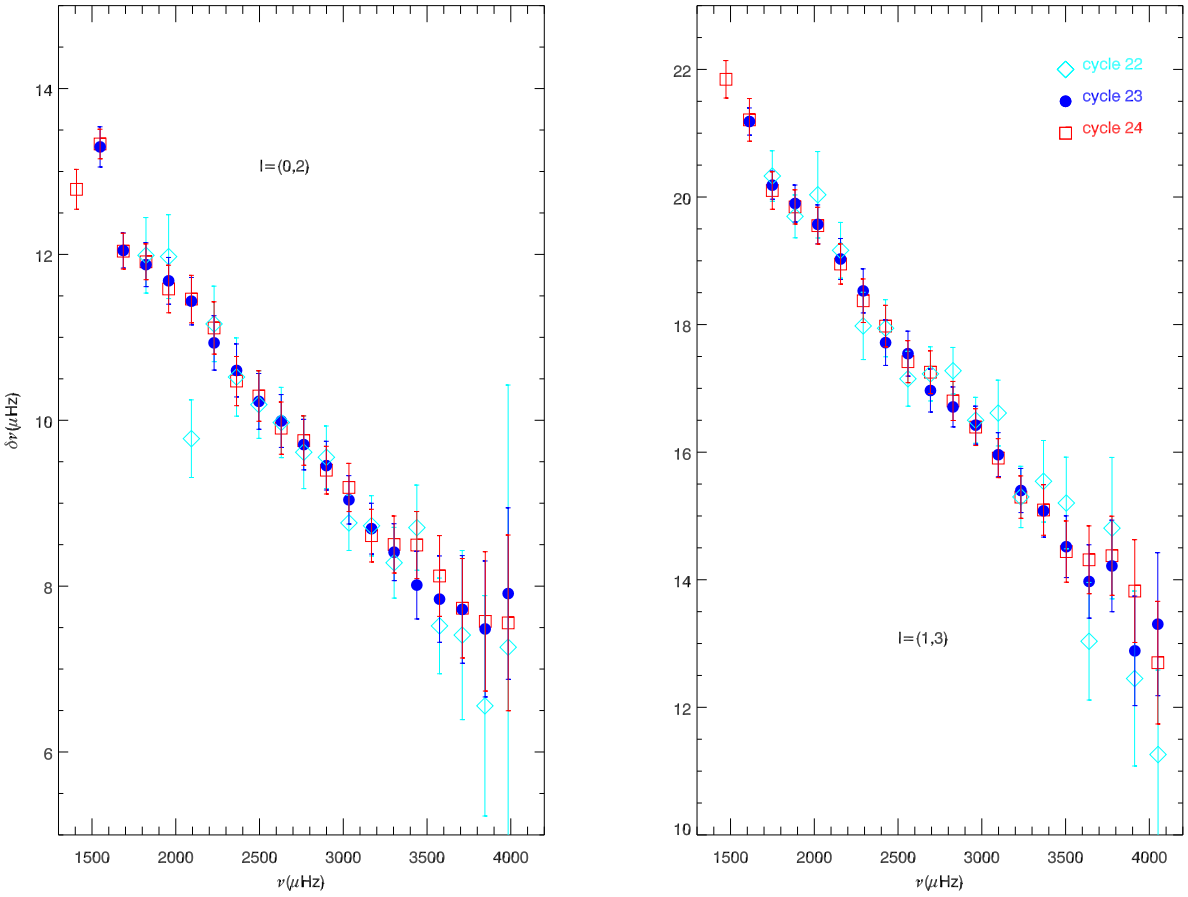

Figure 3.5: The small separations for each minima are shown. Cycle 22 is shown by the light blue diamonds, cycle 23 by the dark blue filled circles and cycle 24 by the red squares. These plots show very little difference between the three solar cycles.

change, suggesting the change here is within the outer layers of the Sun. Figure 3.8 shows the differences between cycles 23 and 24 with the addition of a sine wave (found by visual inspection) to aid the eye.

An abrupt change within the Sun will affect the waves which pass through that part of our star. This change will affect the way the wave oscillates in a similar manner to changing the density of a piece of oscillating string. This change can be thought of as fixing a bead to the piece of string so that it is unable to move along the string. As this bead will make part of the string heavier than the rest it will have a damping effect on the oscillations and cause a slight change in the frequencies of the overtones at which the string oscillates. The effect that this bead will have will depend on its position along the string and the mode in which the string is oscillating. If the bead is added at a node then it will not have a significant effect as that part of the string is not displaced by the oscillation. In contrast to this if the bead is placed at an anti-node where a large displacement is seen the damping effect will be much larger. It is this dependence on frequency that produces the periodic change in the frequency difference. A mathematical derivation of this is shown in Appendix A.

To find the depth at which this difference occurs we compare the frequency changes to two different solar models BP04 (Bahcall & Pinsonneault, 2004) and S (Christensen-Dalsgaard et al., 1996). A localised change in either sound speed, c, density, ρ, or the adiabatic exponent, Γ_1 was applied at different depths to the models. The first adiabatic exponent is defined as the logarithmic derivative of pressure with respect to density at constant entropy. This was performed by integrating over kernels multiplied by the change represented as a Gaussian centred at the depth to be tested (Equation 3.3). Kernels are functions produced by the models which show how changes in parameters relate to changes in frequency. Oscillations within the Sun have nodes and anti-nodes in the same way as the example of the string, so when this change occurs near a node there will be less of

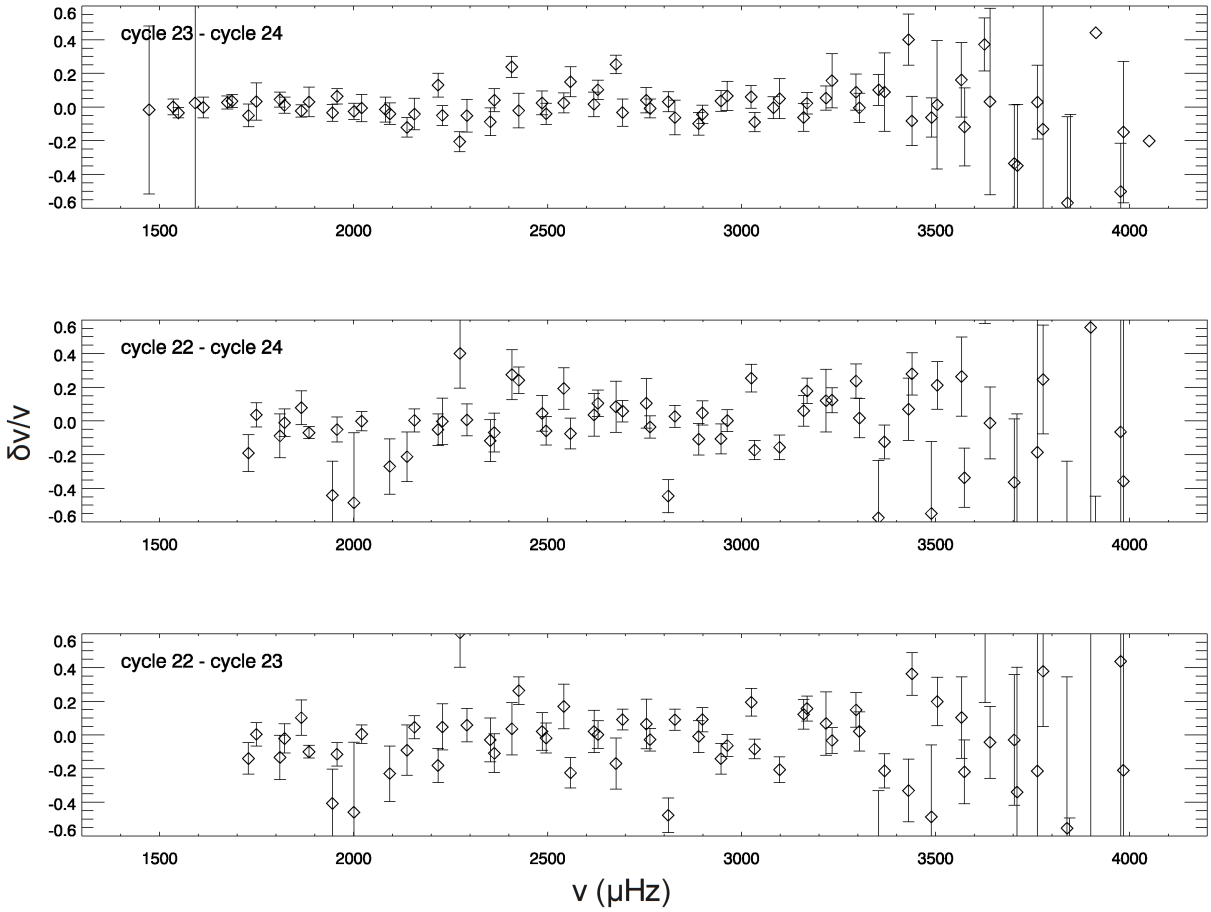

Figure 3.6: Differences in low degree mode frequencies observed for the solar minima by the BiSON project. These differences have been calculated using two year data sets.

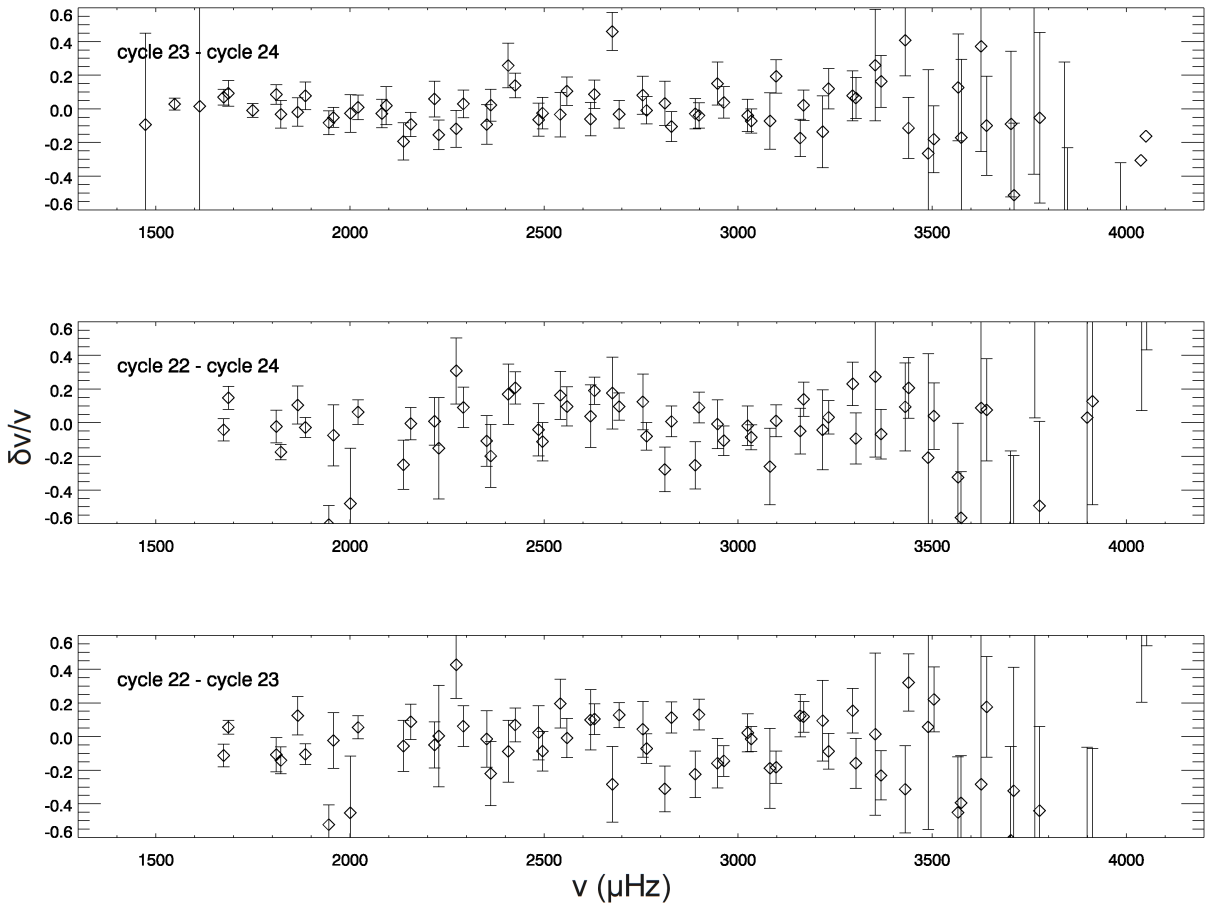

Figure 3.7: Differences in low degree mode frequencies observed for the solar minima by the BiSON project. These differences have been calculated using one year data sets.

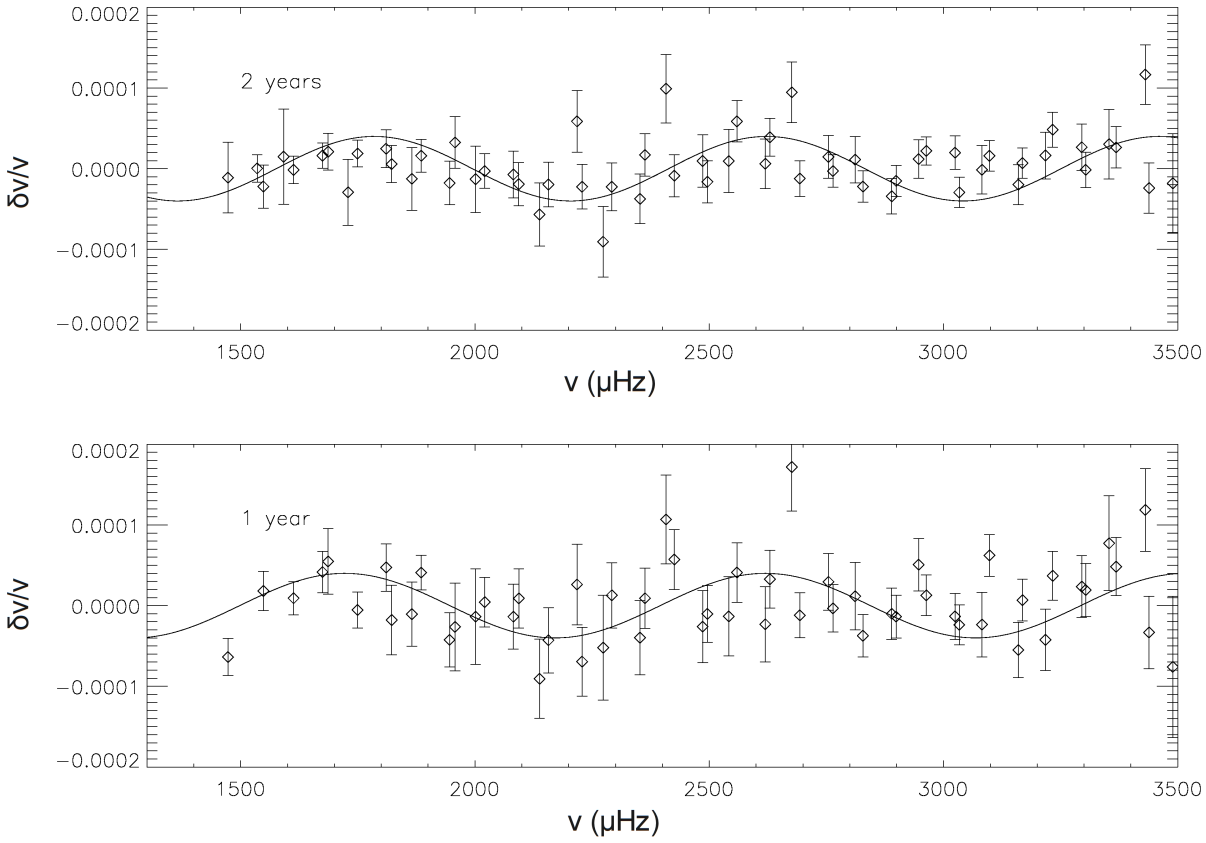

Figure 3.8: The differences between minima for cycles 23 and 24 for the two year dataset (top) and one year dataset (bottom) with a trend line added to aid the eye.

an effect than when the change occurs near an anti-node. The equation to describe the change in frequency seen when the change is applied to the model is shown here for a change in sound speed:

$$\frac{d\nu}{\nu} = \int \kappa(l, n, r) \frac{\delta c(r)}{c(r)} dr. \tag{3.3}$$

Here ν is the frequency of the oscillation, κ represents kernels in (ℓ, n and radius, r) and c is the sound speed. Changing the position at which this Gaussian is centred will test the effect of perturbations centred at different depths. Information on the physical parameters of the change can be extracted from the amplitude of the signal but here we will concentrate on finding the depth at which the change occurs.

The errors in the data collected for cycle 22 are much larger than those for the other two cycles so only the differences between cycles 23 and 24 have been used. To find a first estimate of the fractional depth a comparison between the observed data and the model data was performed by eye. The best fractional depths found can be seen in Figures 3.9 to 3.11. These best matches were then used as the starting point for a χ^2 minimisation. For the two year data sets the best matches have been found at a fractional radii of 0.987 for Γ_1, 0.986 for sound speed and 0.989 for density. These radii are close to the second helium ionization zone, which sits at $\sim$0.98. The first adiabatic exponent (the logarithmic derivative of pressure with respect to density at constant entropy) is close to 5/3 for most of the solar interior as it is almost an ideal gas. However, Γ_1 is known to deviate from this in the hydrogen and helium ionization zones (Elliott & Kosovichev, 1998). This suggests Γ_1 is the most logical variable to produce a change in the interior.

A more robust way of finding the depth at which a change in Γ_1 can occur could be done by calculating model curves with changes centred at different depths in a range centred on the helium ionization zone and interpolating the data so that $\delta\nu/\nu$ are determined at the same frequencies as the observed data. These curves can then be fitted to the data to find the combination of depths which provide the most accurate fit. This approach

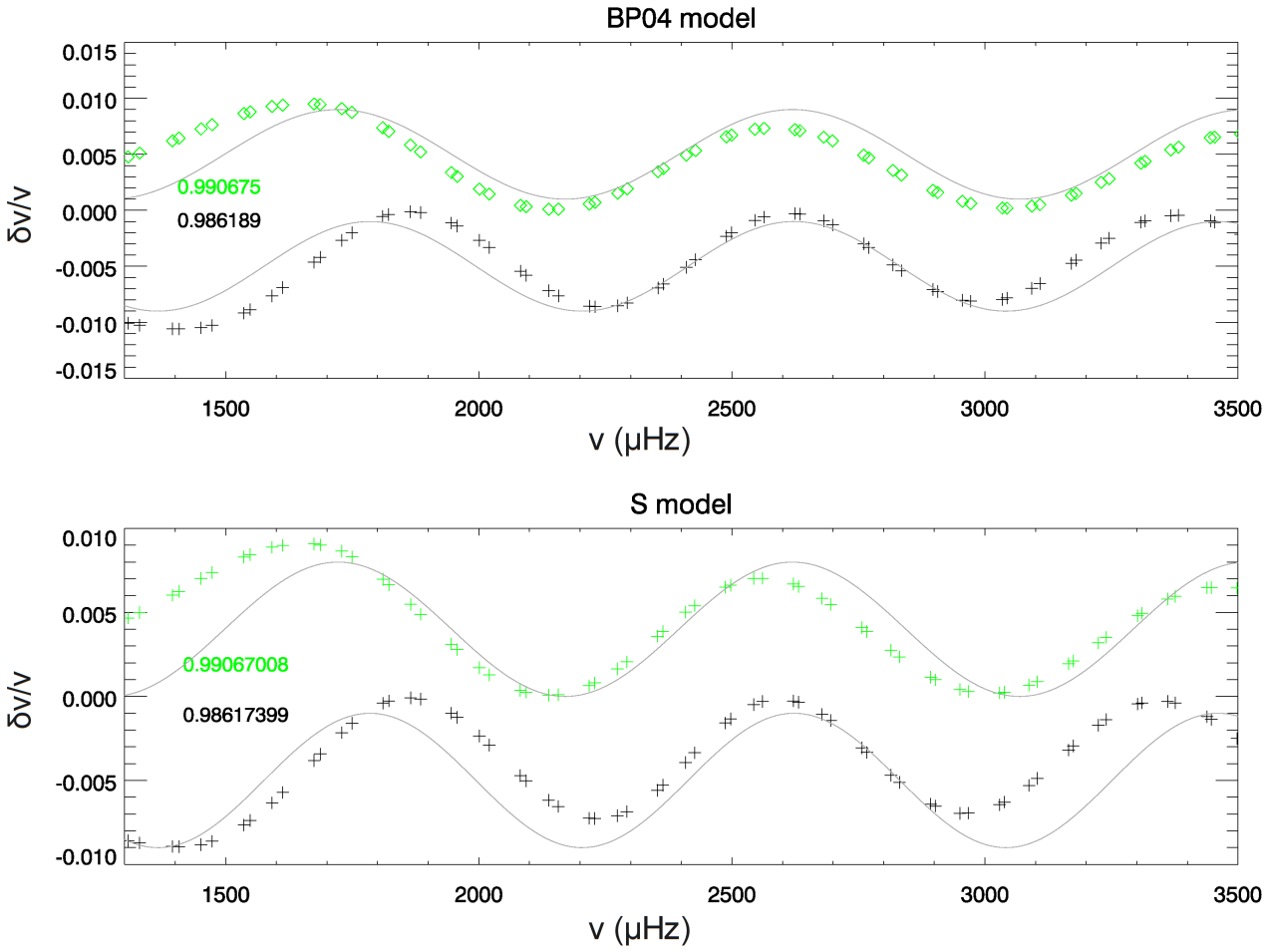

Figure 3.9: Modelled frequency differences when a change is made in Γ_1 centred at a radial depth of 0.986 (to match the two year data set) and 0.992 (to match the one year dataset). Both plots have had the sine curve from Figure 3.8 added for comparison (solid line).

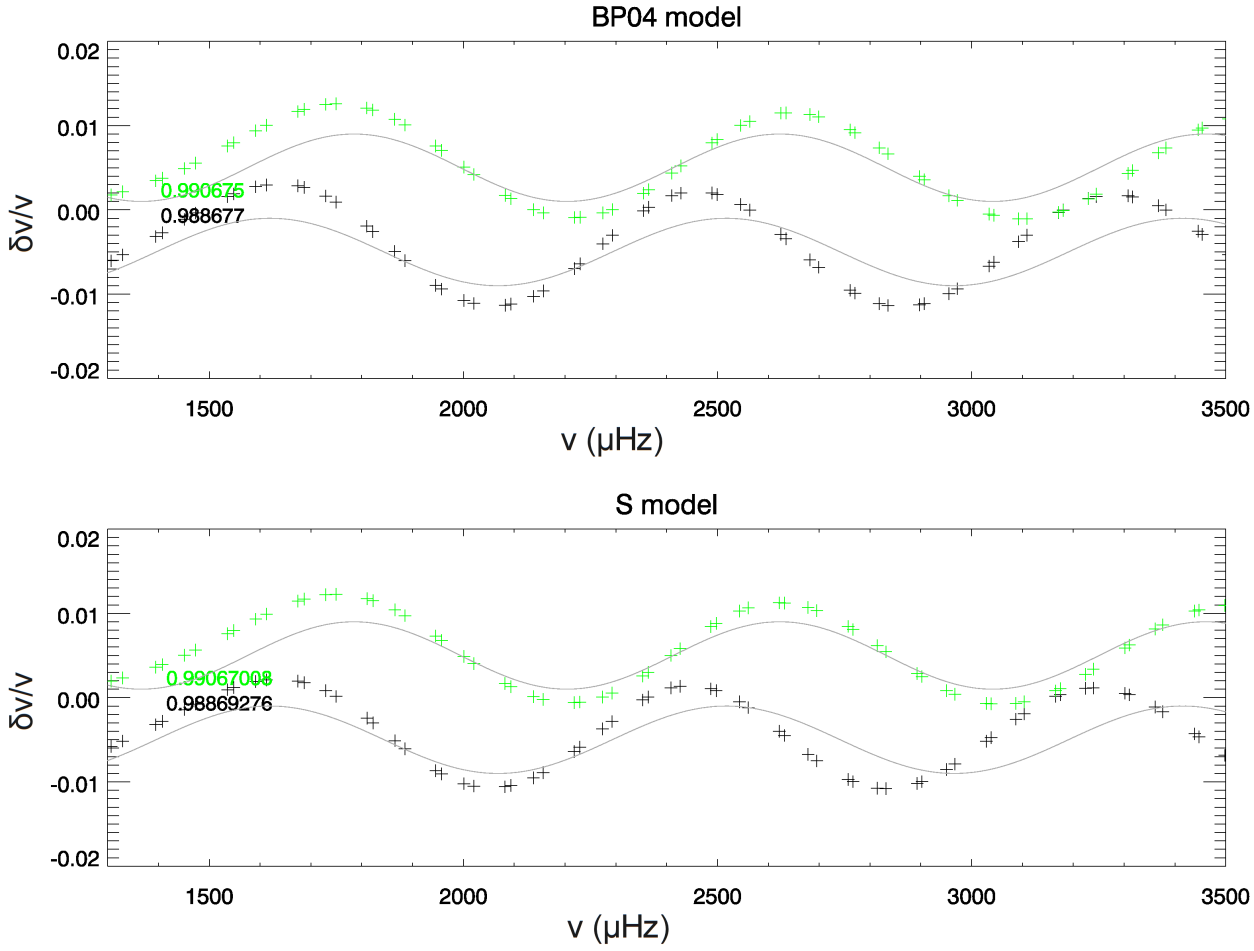

Figure 3.10: Modelled frequency differences when a change is made in density. The top plot shows the change when applied to the BP04 model with the change centred at 0.989 (to match the two year data set) and 0.991 (to match the one year dataset). The bottom plot shows the change when applied to the S model with the change at 0.989 and 0.991 to match the two and one year data sets respectively. Both plots have had the sine curve from Figure 3.8 added for comparison (solid line).

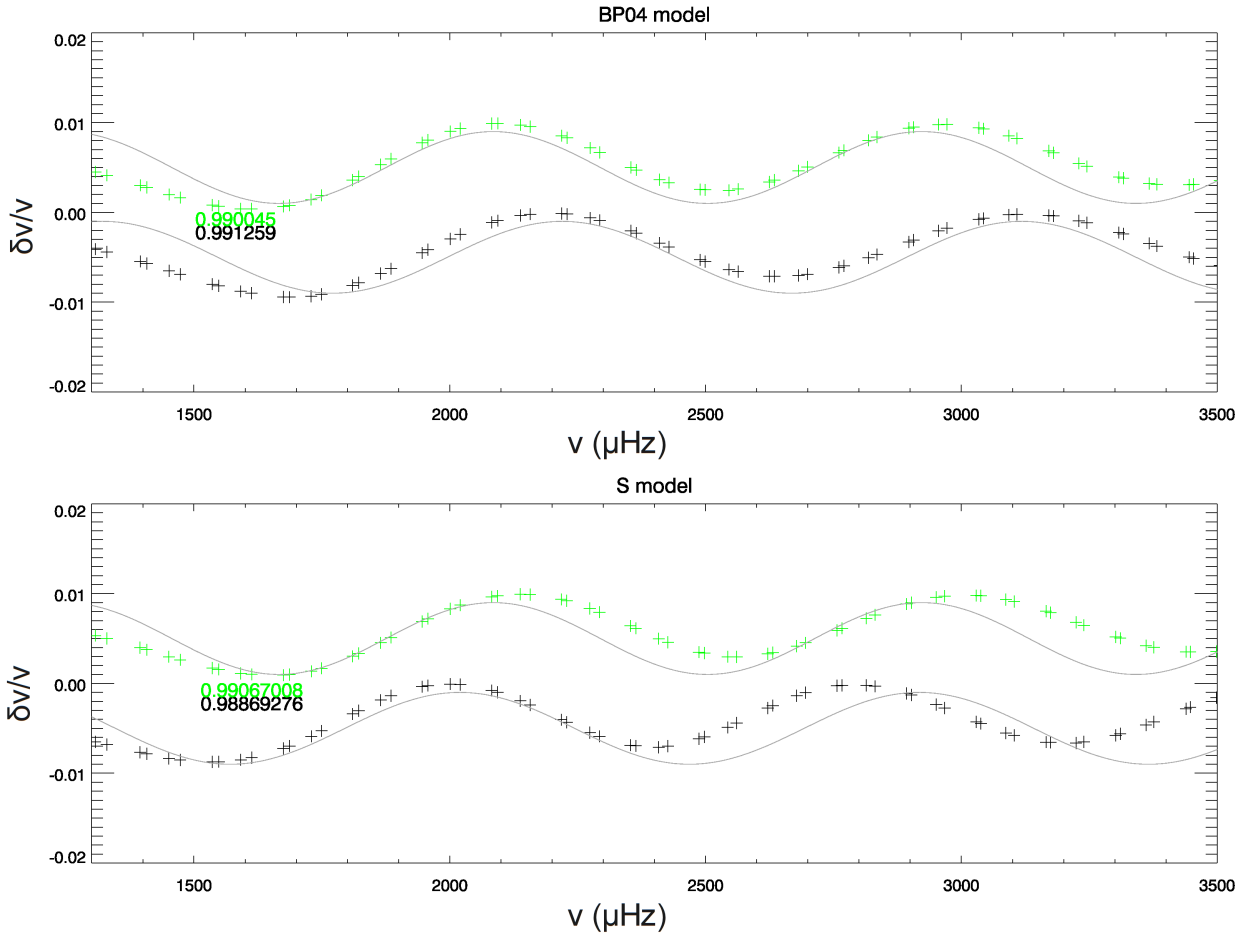

Figure 3.11: Modelled frequency differences when a change is made in sound speed. The top plot shows the change when applied to the BP04 model with the change centred at 0.986189 (to match the two year data set) and 0.991 (to match the one year dataset). The bottom plot shows the change when applied to the S model with the change at 0.986 and 0.991 to match the two and one year data sets respectively. Both plots have had the sine curve from Figure 3.8 added for comparison (solid line).

should also be able to find the shape of any change.

3.3 Conclusion

The most recent solar minimum has been longer and quieter than expected. This can be seen in Sunspot number as well as a number of other activity proxies. To investigate the changes in the Sun that have occurred at the time of this abnormal minimum we have studied oscillation data collect by BiSON over the last 3 solar cycles. When the frequency differences between solar cycles are observed a periodic signature can be seen. Such features are known to be the result of sharp changes within the solar interior. By comparison to model data it has been shown that the changes seen between cycles may be related to a change in Γ_1 in the region of the second helium ionization zone. These findings are consistent with Basu & Mandel (2004) who found evidence of solar structure changes in the region of the helium ionization zone which correlate with changes in solar cycle activity.

Chapter 4

Discussion

This thesis has described two different investigations. The first develops an automated pipeline that is able to distinguish between frequencies produced by modes of oscillations of angular degree $\ell = 0$ and angular degree $\ell = 1$. All the methods that have been tested use different scaling factors to enable the use of comparison techniques where information is gained by comparing stellar properties. The first method uses a multiplicative scale factor to force the two stars to have a comparable large separation. The idea behind this method is that once on the same échelle plot the ridges of the two stars will line up so that corresponding ridges are close together. When this method has been tested on model data we find this is the case 99.8% of the time but this method could have problems when applied to data from real stars, if the two stars have different surface terms then the ridges will not align as expected. To combat this an alternative method has also been explored which arises from the asymptotic relation. This method is less vulnerable to the effects of the surface term and while it shows success by providing accurate identifications in up to 92% of cases, it like the first method require previous knowledge of the radial order of a mode. This can be as difficult to identify as the angular degree. To remove this dependence an alternative offset method has been tested that uses a reduced frequency in place of the frequency. This enables the matches to be performed by frequency rather than radial order. When tested on model data this method does not appear to be as reliable as when knowledge of n is assumed. This appears to be caused by wrap around effects. To deal with this a slightly altered method which constrains the possible values

of the offset has also been developed. When applied to model data this method shows promising results returning to the same levels of success as the original method (99.8%). This last method is the most likely to provide an accurate identification when applied to data from real stars. The method has been tested for worse than expected observations (by reducing the number of frequencies used to perform the identification) and the effects of noise. The method shows resilience to these tests and remains reliable.

To further this investigation the adapted offset method needs to be tested on data collected from observations. When choosing stars to use the method on we would look for stars where only two ridges can be seen. The stellar data could be compared to other stars for which the identification is already known or a similar star from a collection of models. In performing this identification problems could arise if the surface terms of the two stars have different forms. For example the surface term of the Sun increases with increasing frequency. If such a star is compared to one with a flat surface term then the shapes of the ridges of the two stars maybe too different to compare successfully. One way to avoid such effects is to compare the stars to model data where the surface term is not present. The use of models could also prove beneficial as they could provide a more accurate test. By comparing each star to 20 or more different sets of model frequencies, provided the 20 models remain similar to the star, we should be able to identify occasions where an incorrect match has been made.

The methods dependence on the surface term could be used to provide information on the similarity of the surface terms of two stars. Once the identification has been made it will be possible to see if the difference between the two mis-matched offsets is the largest difference. If this is the case then we know the two stars must have similar surface terms.

If this method proves to be as successful on real stars as it is with models it would be worth expanding on the range of stars for which it has been tested. The model frequencies used to test the method in this study have been chosen to follow certain constraints: that

they are from solar-like main sequence stars and that they are pure p-mode oscillations. More evolved stars will not only exhibit p-modes but also mixed modes. These mixed modes can cause avoided crossings on échelle diagrams, where instead of continuing as a single line a ridge is broken and begins again. To deal with ridges of this form a linear or curved fit could be used to fit across the two sections of the ridge and represent it in place of the ridge itself. These tests could also be expanded to red giants where solar like oscillations are also seen.

The second study described in this thesis investigates changes that have occurred in the most recent solar minimum which has been longer and quieter than expected. This can be seen in Sunspot number as well as a number of other activity proxies. To investigate possible causes of this abnormal minimum we have studied oscillation data collect by BiSON over the last 3 solar cycles. When the frequency differences between solar cycles are observed a periodic signature can be seen. Such features are known to be the result of sharp changes within the solar interior. By comparison to model data it has been shown that the changes seen between cycles may be related to a change in Γ_1 in the region of the second helium ionization zone. The second helium ionization zone is already known to produce a similar periodic signature in frequency. Basu & Mandel (2004) have also found evidence of solar structure changes in the region of the helium ionization zone which correlate with changes in solar cycle activity. This investigation has concentrated on using the period of the oscillatory signature to discover the depth of the change. The amplitude of the signatures also provide information on the size of the feature that causes it. This could be investigated by altering the magnitude of the change applied to the model data. The changes observed between minima in this investigation could then be compared to the changes over a solar cycle seen by Basu & Mandel (2004).

During this investigation we have assumed that any change is Gaussian. This assumption could be removed by calculating model curves with changes at depths that cover a

range centred on the helium ionization zone and interpolating the data so that $\delta\nu/\nu$ are determined at the same frequencies as the observed data. These curves would then be fitted to the data to find the combination of depths that provide the most accurate fit. This approach should find the shape of any change as well as it's depth.

Appendix A

Appendix A

The example of a bead on a string is a way to picture a string where the mass per unit length changes part way along its length then returns to the previous value. A diagram illustrating the set up can be seen in Figure A.1 . This piece of string has three sections: section I (between 0 and a) where its mass per unit length is ρ. At a this changes sharply to ρ' (section II) and returns to ρ at b for section III.

The speed of sound in the different regions is given by:

$$c^2 = T/\rho, \tag{A.1}$$

for sections I and III, where T is the tension of the string, and:

$$c'^2 = T/\rho', \tag{A.2}$$

Figure A.1: Illustration of inhomogeneous string.

for section II. This change in sound speed will cause the wavelengths, λ, (and hence wave numbers) in the different regions to be different, although the frequency, ν and angular frequency, $\omega = 2\pi\nu$, must remain constant. The magnitude of the angular wave numbers will be given by:

$$k = 2\pi/\lambda = \omega/c, \tag{A.3}$$

and

$$k' = 2\pi/\lambda' = \omega/c'. \tag{A.4}$$

Consider a wave travelling from left to right, neglecting reflections at the end points. In region I there is an incoming wave from the left and a reflected wave from the boundary with region II, so the wave form will be:

$$\Psi_I(x,t) = e^{i(\omega t - kx)} + Re^{i(\omega t + kx)}. \tag{A.5}$$

In region II there will again be transmitted and reflected waves

$$\Psi_{II}(x,t) = Ae^{i(\omega t - k'x)} + Be^{i(\omega t + k'x)}. \tag{A.6}$$

In region III there will only be the right travelling wave from the boundary with II.

$$\Psi_{III}(x,t) = Se^{i(\omega t - kx)}. \tag{A.7}$$

R, A, B and S are complex reflection and transmission coefficients. To determine

these we need the following boundary conditions:

$$\Psi_I(a,t) = \Psi_{II}(a,t), \tag{A.8}$$

$$\Psi_I I(b,t) = \Psi_{III}(b,t), \tag{A.9}$$

$$\frac{d\Psi_I}{dx}(a,t) = \frac{\Psi_{II}}{dx}(a,t), \tag{A.10}$$

$$\frac{d\Psi_I I}{dx}(b,t) = \frac{\Psi_{III}}{dx}(b,t), \tag{A.11}$$

The first two boundary conditions assure that the string is continuous. The third and fourth assume that the gradient of the string is continuous, which shows there are no unresolved forces. The boundary conditions required for a standing wave are:

$$\Psi_I(0,t) = 0, \tag{A.12}$$

$$\Psi_{III}(L,t) = 0. \tag{A.13}$$

When the wave forms are solved for these boundary conditions we obtain:

$$A = -2k(k+k')e^{-ia(k-k')}e^{2ik'b}\tilde{K}, \tag{A.14}$$

$$B = 2k(k-k)e^{ia(k-k')}\tilde{K}, \tag{A.15}$$

$$R = (k^2 - k'^2)(e^{2ik'a} - e^{2ik'b})e^{-2ika}\tilde{K}, \tag{A.16}$$

$$S = -4kk'e^{ia(k'-k)}e^{ib(k'+k)}\tilde{K}, \tag{A.17}$$

where

$$\tilde{K} = \left[e^{2ik'a}(k-k')^2 + e^{2ik'b}(k+k')^2\right]^{-1}. \tag{A.18}$$

The equations for the three regions can now be re-written as

$$\Psi_I(x,t) = 2\sin(\omega t)\left\{\sin(kx) - R_0\,\sin(kx+\theta_R)\right\}, \tag{A.19}$$

$$\Psi_{II}(x,t) = 2\sin(\omega t)\left\{A_0\ \sin(k'x - \theta_A) - B_0\ \sin(k'x + \theta_B)\right\}, \tag{A.20}$$

$$\Psi_{III}(x,t) = 2\sin(\omega t)\left\{S_0\ \sin(kx - \theta_S)\right\}, \tag{A.21}$$

where the complex coefficients described in Equations A.14 to A.17 have been rewritten in the form

$$R = R_0 e^{i\theta_R}, \qquad A = A_0 e^{i\theta_B}, \qquad B = B_0 e^{i\theta_B}, \qquad S = S_0 e^{i\theta_S}. \tag{A.22}$$

In the case of a homogeneous string, fixed at both ends the frequency of successive standing waves is given by:

$$\omega_n = ck_n = c\frac{n\pi}{L}. \tag{A.23}$$

In the case of our inhomogeneous string the region of different density causes each standing mode to experience a phase shift which breaks the boundary condition $\Psi_I = 0$. This can be solved by calculating the phase shift require to fix $\Psi_I = 0$. This shift can calculated from Equation A.19 as:

$$\alpha = \frac{1}{k}\arctan\left(\frac{R_0\sin\theta_R}{1 - R_0\cos\theta_R}\right). \tag{A.24}$$

To satisfy the fixed boundary condition at $x = L$, we require that $\Psi_{III}(L + \alpha, t) = 0$. This reduces to solving (for ω_n)

$$S_0\ \cos\ \theta_S\ \sin\left(\frac{\omega_n}{c}(L+\alpha)\right) - S_0\ \sin\ \theta_S\ \cos\left(\frac{\omega_n}{c}(L+\alpha)\right) = 0. \tag{A.25}$$

References

Appourchaux T., Rabello-Soares M. C., Gizon L., 1998, *Astronomy and Astrophysics*, 132, 121

Appourchaux T., et al., 2008, *Astronomy and Astrophysics*, 488, 705

Aharmin B., et al., 2008, *Phys. Rev. Lett.*, 101, 111301

Ahmad Q.R., et al., 2001, *Phys. Rev. Lett.*, 87, 071301

Bahcall J. N., Pinsonneault M. H., 2004, *Physical Review Letters*, 92, 121301

Basu S., Antia H.M., Narasimha D., 1993, *Bulletin of the Astronomical Society of India*, 21, 669

Basu S., Antia H. M., 2004, *The Astrophysical Journal*, 606, 85

Basu S., Antia H. M., 2004, *The Astrophysical Journal*, 617, L155

Basu S., Chaplin W. J., Elsworth Y., 2010, *The Astrophysical Journal*, 710, 1596

Bedding T. R., Kjeldsen H., 2003, *Publications of the Astronomical Society of Australia*, 20, 203

Bedding T. R., Kjeldsen H., 2010, *CoAst*, 161, 3

Borucki W. J., et al. 2006, *American Astronomical Society Meeting*, 38, 1071

Broomhall A.-M., Chaplin W. J., Elsworth Y., Fletcher S. T., New R., 2009, *The Astrophysical Journal*, 700, 162

Broomhall A.-M., Chaplin W. J., Elsworth Y., Simoniello, R., 2012, *Monthly Notices of the Royal Astronomical Society*, 420, 1405

Brown T. M., Gilliland R. L., Noyes R. W., Ramsey L. W., 1991, *Astrophysical Journal*, 368, 599

Burent J., 1928, Platonism, *Berkeley:University of California Press*, p.103-104

Chaplin W. J., et al., 1996, BiSON Performance, *Solar Physics*, 168, 1

Chaplin W. J., Christensen-Dalsgaard, J., Elsworth, Y., Howe, R., Isaak, G. R., Larsen, R. M., New, R., Schou, J., Thompson, M. J., Tomczyk, S., 1999, *Monthly Notices of the Royal Astronomical Society*, 308, 405

Chaplin W.J., Elsworth Y., Isaak G. R., Miller B. A., New R., 2004, *Monthly Notices of the Royal Astronomical Society*, 352, 1102

Chaplin, W. J., Elsworth, Y., Miller, B. A., Verner, G. A., New, R., 2007, *The Astrophysical Journal*, 659, 2, 1749

Christensen-Dalsgaard J., Gough D. O., Thompson M. J., 1991, *The Astrophysical Journal*, 378, 413

Christensen-Dalsgaard J., 1993, *Proceedings of GONG 1992: Seismic Investigation of the Sun and Stars, Astronomical Society of the Pacific Conference Series*, 42, 347

Christensen-Dalsgaard J., et al., 1996, *Science*, 272, 1286

Christensen-Dalsgaard J., 2003, *Lecture Notes of Stellar Oscillations*, chapter Excitation and Damping of the Ocillations, Arhus University, 5th edition

Claverie A., Isaak G. R., McLeod C. P., van der Raay H. B., Cortes T. R., 1979, *Nature*, 282, 591

Cox J. P., Giuli R. T., 1968, Principles of stellar structure, *Gordon and Breach*

Deubner, F.-L., 1975, *Solar Physics*, 40, 1975, 333

Davis R., Harmer D. S., Hoffman K. C., 1968, *Physical Review Letters*, 20, 1205

Delahaye F., Pinsonneault M. H., 2006 *The Astrophysical Journal*, 649, 1, 529

Demarque P., Woo J.-H., Kim Y.-C., Yi S.K., 2004, *The Astrophysical Journal Supplement Series*, 155, 667

Eddy J.A., 1976, *Science*, 192, 1189

Elliott J.R., Kosovichev A.G., 1998, *The Astrophysical Journal*, 500, 199

Elsworth Y., Howe R., Isaak G. R., McLeod C. P., New R., 1990, *Nature*, 347, 536

Elsworth Y., Howe R., Isaak G. R., McLeod C. P., Miller B. A., van der Raay H. B., Wheeler S. J., New R., 1995, *Proceedings of GONG '94: Helio- and Astero-Seismology from the Earth and Space, Astronomical Society of the Pacific Conference Series*, 76, 392

Fletcher S. T., Broomhall A.-M., Salabert D., Basu S., Chaplin W. J., Elsworth Y., Garcia R. A., New R., 2010, *The Astrophysical Journal*, 718, 19

Fröhlich C., et al., 1995, *Solar Physics*, 162, 1-2, 101

Gabriel A. H., et al., 1995, *Solar Physics*, 162, 1, 61

Galileo G, 1613, Istoria e Dimostrazioni Intorno Alle Macchie Solari e Loro Accidenti (History and Demonstrations Concerning Sunspots and their Properties), Rome

García R. A., et al., 2004, *Solar Physics*, 220, 269

García R. A., Turck-Chize S., Jiménez-Reyes S. J., Ballot J., Pallé P. L., Eff-Darwich A., Mathur S., Provost J., 2007, *Science*, 316, 1591

Gilliland R. L. et al., 2010, *Publications of the Astronomical Society of the Pacific*, 122, 131

Goode P. R., Gough D., Kosovichev A. G., 1992, *Astrophysical Journal*, 387, 707

Gough D. O., 1990, *Progress of Seismology of the Sun and Stars, Proceedings of the Oji International Seminar*, 367, 283

Gough D.O., 1977, *The Astrophysical Journal*, 214, 196

Grec G., Fossat E., Pomerantz M. A., 1983, *Solar Physics*, 82, 55

Gruberbauer M., Kallinger T., Weiss W. W., Guenther D. B., 2009, *Astronomy and Astrophysics*, 506, 1043

Grundahl F., Arentoft T., Christensen-Dalsgaard J., Frandsen S., Kjeldsen H., Rasmussen P. K., 2008, *Journal of Physics: Conference Series*, 118, 012041

Hale G. E., 1924, *Nature*, 113, 105

Harvey J. W., et al., 1996, *Science*, 272, 1284

Hathaway D. H., Wilson R. M., Reichmann E. J., 1999, *Journal of Geophysical Research*, 104, 22

Hathaway D. H., 2011, *Solar Physics*, 273, 221

Hekker S., Basu S., Elsworth Y., Chaplin W. J., 2011, *Monthly Notices of the Royal Astronomical Society*, 418, L119

Howe R., Komm R. W., Hill, F., 2002, *The Astrophysical Journal*, 580, 1172

Jian L. K., Russell C. T., Luhmann J. G., 2011, *Solar Physics*, 274, 321

Jiménez-Reyes S. J., Garcia R. A., Chaplin W. J., Korzennik S. G., 2004, *The Astrophysical Journal*, 610, 65

Kjeldsen H., Bedding T. R., 1995, *Astronomy and Astrophysics*, 293, 87

Kolmogorov A., 1956, Foundations of the Theory of Probability (2nd ed.). *New York: Chelsea*, ISBN 0828400237

Komm, R., Howe, R., Hill, F., 2002, *The Astrophysical Journal*, 572, 1

Kosovichev, A. G. et al., 1997, *Solar Physics*, 170, 43

Fröhlich C., et al., 1997, *Solar Physics*, 170, 1

Leighton R. B., Noyes R. W., Simon, G. W., 1962, *The Astrophysical Journal*, 135, 474

Lemaire P., 1991, *Advances in Space Research*, 11, 169

Michel E., et al., 2008, *Science*, 322, 558

Montgomery M. H., 2011, *Science*, 332, 180

Pesnell W. D., 2008, *Solar Physics*, 252, 209

Antia1 H. M., Basu S., 2010, *Astrophysical Journal*, 720, 494

Roshchina E. M., Sarychev A. P., 2011, *Solar System Research*, 45, 365

Roxburgh I.W., Vorontsov S.V., 1994, *Monthly Notices of the Royal Astronomical Society*, 268, 880

Salabert, D., Jiménez-Reyes, S. J., Tomczyk, S., 2003, *Astronomy and Astrophysics*, 408, 729

Salabert D., García R. A., 2009, *Proceedings of GONG 2008: Solar-Stellar Dynamos as Revealed by Helio- and Asteroseismology, Astronomical Society of the Pacific Conference Series*, 416, 329

Schatten K. H., Scherrer P. H., Svalgaard L., Wilcox J. M. , 1978, *Geophysical Research Letters*, 5, 411

Schou J., et al., 2012 *Solar Physics*, 275, 229

Schwabe M., 1843, *Astronomische Nachrichten*, 20, 283

Serenelli A. M., Haxton W. C., Peña-Garay C., 2011, *The Astrophysical Journal*, 743, 24

Tapping K. F., 1987, *Journal of Geophysical Research*, 92, 829

Tassoul M., 1980, *Astrophysical Journal*, 43, 469

Walker G., et al. 2003, *Publications of the Astronomical Society of the Pacific*, 115, 1023

Wolf R., 1877, *München R. Oldenbourg*, 116

Woodard M. F., Noyes R. W., 1985, *Nature*, 318, 449